Key Points:
- Median waves enhance tidal sand transport vectors, whereas extreme waves can dominate sand transport and sometimes induce full reversals
- A new continental shelf classification is presented based on wave-, tide-, and nonlinear wave-tide interaction dominance of sand transport
- Nonlinear wave-tide interactions are a dominant or subdominant contributor to sand transport in extreme conditions and cannot be ignored

Supporting Information:
- Supporting Information S1

Correspondence to:
E. V. King,
erin.king@plymouth.ac.uk

The Impact of Waves and Tides on Residual Sand Transport on a Sediment-Poor, Energetic, and Macrotidal Continental Shelf

E. V. King[1] , D. C. Conley[1] , G. Masselink[1] , N. Leonardi[2] , R. J. McCarroll[1] , and T. Scott[1]

[1]Coastal Processes Research Group, School of Biological and Marine Sciences, Plymouth University, Plymouth, UK, [2]Department of Geography and Planning, School of Environmental Sciences, University of Liverpool, Liverpool, UK

Abstract The energetic, macrotidal shelf off South West England was used to investigate the influence of different tide and wave conditions and their interactions on regional sand transport patterns using a coupled hydrodynamic, wave, and sediment transport model. Residual currents and sediment transport patterns are important for the transport and distribution of littoral and shelf-sea sediments, morphological evolution of the coastal and inner continental shelf zones, and coastal planning. Waves heavily influence sand transport across this macrotidal environment. Median (50% exceedance) waves enhance transport in the tidal direction. Extreme (1% exceedance) waves can reverse the dominant transport path, shift the dominant transport phase from flood to ebb, and activate sand transport below 120-m depth. Wave-tide interactions (encompassing radiation stresses, Stoke's drift, enhanced bottom-friction and bed shear stress, refraction, current-induced Doppler shift, and wave blocking) significantly and nonlinearly enhance sand transport, determined by differencing transport between coupled, wave-only, and tide-only simulations. A new continental shelf classification scheme is presented based on sand transport magnitude due to wave-forcing, tide-forcing, and nonlinear wave-tide interactions. Classification changes between different wave/tide conditions have implications for sand transport direction and distribution across the shelf. Nonlinear interactions dominate sand transport during extreme waves at springs across most of this macrotidal shelf. At neaps, nonlinear interactions drive a significant proportion of sand transport under median and extreme waves despite negligible tide-induced transport. This emphasizes the critical need to consider wave-tide interactions when considering sand transport in energetic environments globally, where previously tides alone or uncoupled waves have been considered.

Plain Language Summary The South West UK has a large tidal range (macrotidal) and is exposed to high-energy waves. We created a numerical model of this region, which calculates waves, tides, and sand transport over time. This was used to investigate the importance of waves, tides, and their interactions on the net movement of sand under different wave and tide states, which is important for evolution of the coastline and coastal planning. Sand transport is heavily influenced by waves. The interaction between waves and tides can contribute more to net sand transport than the summed contributions of waves and tides alone. Storm waves can cause sand movement at depths below 120 m and can reverse sand transport pathways.

1. Introduction

Residual flow and sediment transport patterns have important implications for the transport and distribution of littoral and shelf sea sediments, and for morphological evolution of the coastal and inner continental shelf zones (Leonardi et al., 2015; Lewis et al., 2015; Lin & Falconer, 2001). Shelf sediments are susceptible to wave-driven resuspension and net transport by residual tidal currents and wave asymmetry due to wave shoaling. Net sand transport paths are susceptible to wave action, and can reverse direction during extreme wave events (Pattiaratchi & Collins, 1988). Understanding residual flow patterns and the effect of waves is important for understanding regional sediment transport pathways and is relevant for coastal zone management.

Many previous modeling efforts focus on residual tidal circulation, ignoring surface wave effects on regional sediment transport and morphological evolution. Residual currents are generated by nonlinear advection of momentum, density gradients, bottom friction nonlinearities, wind stress, and nonlinearities in the volume

continuity equation related to Stokes drift (Uncles, 1982, 2010; Zimmerman, 1978). Pingree and Griffiths (1979) modeled tide-induced bed shear stress around the British Isles qualitatively matching mean and maximum bed shear stress vectors to sand transport paths described by Stride (1963). Recently, Leonardi and Plater (2017) focus on tidally induced morphodynamic equilibrium of the South East UK coastline and potential long-term morphological evolution.

However, surface waves increase bed shear stress, enhancing sediment resuspension and enabling (enhancing) suspended sediment transport by weak (strong) tidal currents. Interactions between water level variations and combined steady tidal flow and wave-driven oscillatory flow and the bed influence suspended and bed load sediment transport (Damen et al., 2018; Harris & Collins, 1991; Porter-Smith et al., 2004; van der Molen, 2002; van Rijn, 2007a, 2007b). For equivalent current magnitudes, wave-induced bed shear stresses are larger than for tidal currents due to the thinner wave boundary layer (Nielsen, 1992). Wave-current interactions nonlinearly enhance the bed shear stress and apparent roughness due to the interaction between wave and current bottom boundary layers (Kemp & Simmons, 1982, 1983; Klopman, 1994; Umeyama, 2005). The relative incident wave angle to the steady flow influences the vertical current profile and variation in apparent bed roughness, demonstrated by analytical and numerical models (Fredsøe, 1984; Grant & Madsen, 1979, 1986; Olabarrieta et al., 2010; Tambroni et al., 2015). With significant positive trends observed in global 99th percentile wave heights from 1991 to 2008 in buoy and altimeter data (Young et al., 2011), and upward trends in storminess across central, western, and northern Europe (Castelle et al., 2018; Donal et al., 2011), understanding the effect of waves on shelf sediment transport is potentially of increasing importance to coastal communities.

Studies of shelf-scale sediment transport are considering wave-tide coupling more regularly (Dietrich et al., 2011; Hashemi et al., 2014; Moriarti et al., 2014; Xu et al., 2016; Zhang et al., 2016); however, coupled modeling systems are more computationally expensive. A number of studies consider uncoupled tides and waves as an approximation, ignoring wave-tide interactions (e.g., Bricheno et al., 2015; Neill et al., 2010; Porter-Smith et al., 2004; van der Molen, 2002; Xing et al., 2012). Evidence of wave impacts have been observed across the South West UK continental shelf to depths of 150 m, indicating that wave-tide interactions must be considered when considering regional sand transport pathways (Channon & Hamilton, 1976; Reynaud et al., 1999; Thompson et al., 2017); however, the extent of wave influences on sediment transport across the continental shelf is not fully understood.

A challenge in understanding regional sand transport patterns is the spatial and temporal limitations of observational campaigns to capture flow patterns at sufficient resolution and time scales, and their susceptibility to local effects (Stride & Belderson, 1990). This results in uncertainties in regional-scale residual circulations and uncertainty regarding the relative importance of different processes such as surface waves, wind, and baroclinic effects. Modeling can overcome spatial and temporal limitations provided that sufficient observational data are available for calibration and validation.

The South West UK presents ideal conditions for examining the effect of waves and tides on sand transport due to its macrotidal regime and highly energetic waves. This paper aims to determine under what conditions waves, tides and their interactions exert an important influence on regional sand transport pathways. Specifically, the following objectives will be investigated: (i) categorization of the spatially varying contributions of waves and tides to potential sand transport using a validated coupled hydrodynamic, sediment transport, and wave model, with applications for other exposed, macrotidal coastlines; (ii) comparison of potential sand transport pathways, major partings, and convergences to known sediment size distributions and observed bedforms to verify the potential sand transport approach; (iii) understanding of the conditions where waves change or reverse sand transport pathways relative to tides alone; and (iv) quantification the contribution and importance of nonlinear wave-tide interactions to potential sand transport in a macrotidal environment.

2. Study Area

The South West UK peninsula, situated on the Northwest European Continental Shelf, comprises several distinct regions with different hydrodynamic/wave regimes (Figure 1). The Approaches extend from the western boundary in the Celtic Sea to a border with the Bristol Channel (northeast) and English Channel (southeast). The North Coast stretches from Hartland Point to Land's End. The Bristol Channel extends
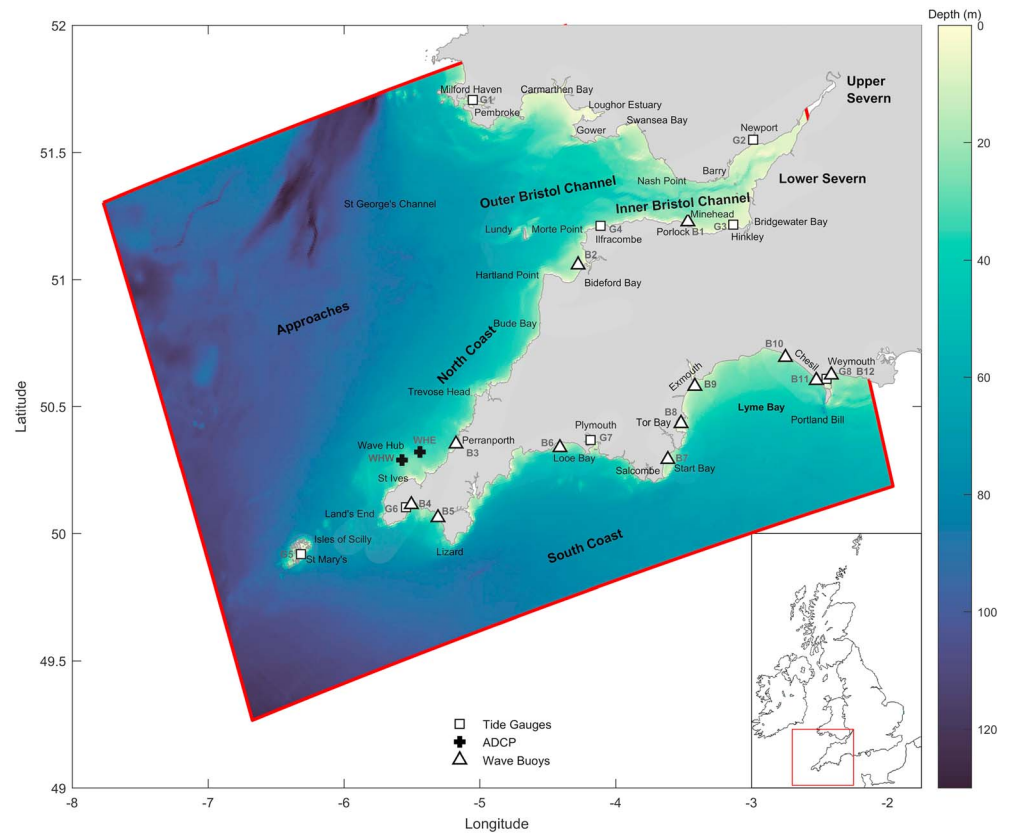
Figure 1. Map of the South West UK continental shelf area considered in this study. Regions are designated as the "Approaches," "Bristol Channel," "North Coast," and "South Coast." The Bristol Channel is further subdivided into "Outer/Inner Bristol Channel" and "Lower Severn." The model domain is shown with model bathymetry, open boundaries (red lines), and validation locations: ADCP deployments (cross), wave buoys (triangle), and tide gauges (square).

from its mouth (spanning Hartland Point to Pembroke) to the upper reaches of the Severn Estuary. The South Coast extends east into the English Channel from Land's End.

2.1. Hydrodynamics

The Bristol Channel experiences the second-largest tidal range globally (mean spring tidal range (MSTR) >12 m in the Upper Severn) due to amplification of the dominant M2 and quarter-wave resonances of the M4 and MS4 tides (Fong & Heaps, 1978; Taylor, 1921; Uncles, 1984). Maximum currents in the Upper Bristol Channel exceed 2.5 m/s, with currents approaching 1 m/s in bays (Collins et al., 1979; Uncles, 1984, 2010; Xia et al., 2010). Resonance contributes to large tidal amplitudes shelf-wide, with a North Coast MSTR exceeding 5 m (>7 m at Hartland Point; Uncles, 2010). Peak currents in the Approaches reaching 0.9 m/s rework sediments year-round (Carruthers, 1963; Heathershaw et al., 1987; Reynaud et al., 1999; Thompson et al., 2017). The South Coast has a lower MSTR (4–5 m), while a degenerate amphidromic point, complex bathymetry, coastal configuration, and nonlinear effects in the equations of motion cause a lower MSTR (2−3 m) and double low water at Weymouth (Pingree & Maddock, 1977; Uncles, 2010). The region experiences pronounced spring-neap variability, with much weaker neap currents (Pattiaratchi & Collins, 1988; Thompson et al., 2017; Uncles, 2010). A northeast residual current flows along the North Coast, with a weak, variable residual in the Approaches (Pingree & Le Cann, 1989). Nonlinear advection of momentum dominates the residual in the Bristol Channel (Holt et al., 2001; Uncles, 1982).

2.2. Waves

The region is exposed to Atlantic waves with potential fetch lengths of 6,000 km (Collins, 1987). The 1% exceedance H_s at Sevenstones (off Land's End) from 2008 to 2014 was 5.9 m and nearshore winter storm H_s along the North Coast can often exceed 6 m (Scott et al., 2016). Average H_s near the shelf break

is ~2 m, reducing to ~1.5 m and below in the Bristol Channel (Bricheno et al., 2015; Pattiaratchi & Collins, 1988; Reynaud et al., 1999). H_s and T_p increase during winter (October–March). Peak near-bed orbital velocities are caused by storm swell with typical storm durations of 24 hr, and can approach 1 m/s below 100-m depth, exceeding critical sand resuspension thresholds (Draper, 1967; Hadley, 1964; Pattiaratchi & Collins, 1988; Reynaud et al., 1999; Thompson et al., 2017). Valiente et al. (2019) show that sheetflow conditions may occur around 30–40-m depth under extreme storm conditions. The region has been subject to a significant increase in extreme (99th percentile) H_s of 1% per annum, among the largest increases observed globally, and an increase in winter H_s and interannual variability associated with the North Atlantic Oscillation and West European Pressure Anomaly indexes (Castelle et al., 2017, 2018; Young et al., 2011). Positive West European Pressure Anomaly values result in higher wave heights south of 52°N and increased storm clustering (Castelle et al., 2017; Hanley & Caballero, 2012; Scott et al., 2016).

2.3. Sand Transport

The presence of a Bristol Channel bed load parting has been debated (Harris & Collins, 1991; Stride & Belderson, 1990, 1991), and uncertainty remains regarding its nature (Lewis et al., 2015; McLaren et al., 1993). Weak convergences and partings are present on the South Coast (Pingree & Griffiths, 1979). Modeling indicates northeast residual sand transport along the North Coast (Holt et al., 2001; Pingree & Griffiths, 1979; Uncles, 2010). Physical sediment characteristics are more important than biological factors for determining bed stability in the Celtic Sea (Thompson et al., 2017). Ward et al. (2015) show regional bed shear stress patterns at 1.1-km resolution. This and aforementioned modeling studies focus on tide-induced bed shear stress, neglecting surface waves.

Observations indicate that waves can strongly influence residual sand transport magnitude and direction, including inducing full reversals (Collins, 1987; Lewis et al., 2015; Pattiaratchi & Collins, 1988; Reynaud et al., 1999). Beach response in this region to extreme waves is well documented (Burvingt et al., 2017; Masselink et al., 2015; Scott et al., 2016). There remains a need to place these observations into regional context, examining the influence of waves on sand transport pathways considering different wave and tidal conditions. Regional-scale residual currents, net sand transport, and the impacts of different wave conditions are not yet described for the Celtic Sea at high resolution.

3. Methods

3.1. Numerical Model

A depth-averaged hydrodynamic, sediment transport, and morphological model coupled to a SWAN third-generation spectral wave model was created using Delft3D for the region shown in Figure 1. A model schematic is also shown in Figure 2. Depth-averaged hydrodynamics are calculated using the unsteady shallow-water equations, following the Boussinesq approximation with the vertical momentum equation reduced to the hydrostatic pressure relation, assuming that vertical accelerations are small relative to gravitational acceleration (Lesser et al., 2004). This study considers conditions typical of winter, where stratification is weak with little near-bed effect (Holt et al., 2001). Consequently, depth-averaged hydrodynamics were considered adequate in line with previous modeling approaches in the region (Bricheno et al., 2015; Holt et al., 2001; Lyddon et al., 2018; Pingree & Griffiths, 1980; Pingree & Le Cann, 1989; Uncles, 1982, 2010; Xia et al., 2010). The effect of secondary flow generation due to a rotating current field on the depth-averaged flow is included by addition of a correction term to the depth-averaged momentum equations, assuming a logarithmic velocity profile, where spiral motion intensity is described by a depth-averaged advection-diffusion equation (Deltares, 2014; Kalkwijk & Booij, 1986). Delft3D uses SWAN, packaged as Delft3D-WAVE, a third-generation phase-averaged wave model based on fully spectral representation of the action balance equation, accounting for wave-current interaction through radiation stress, refraction, wind generation, whitecapping, nonlinear wave-wave interactions, bottom dissipation, and depth-induced breaking (Booij et al., 1999). More details on wave-tide interactions in Delft3D are presented in section 3.2.

Holt et al. (2017) indicate that a resolution of 1.5 km is necessary to be eddy resolving over ~70% of the coastal ocean areas globally, and 1.5 km was considered sufficient for resolving the internal Rossby radius on the Northwest European shelf in the development of the operational AMM15 model (Graham et al., 2018). A hydrodynamic resolution of 1 km was used in this study, on a curvilinear, spherical coordinate grid.
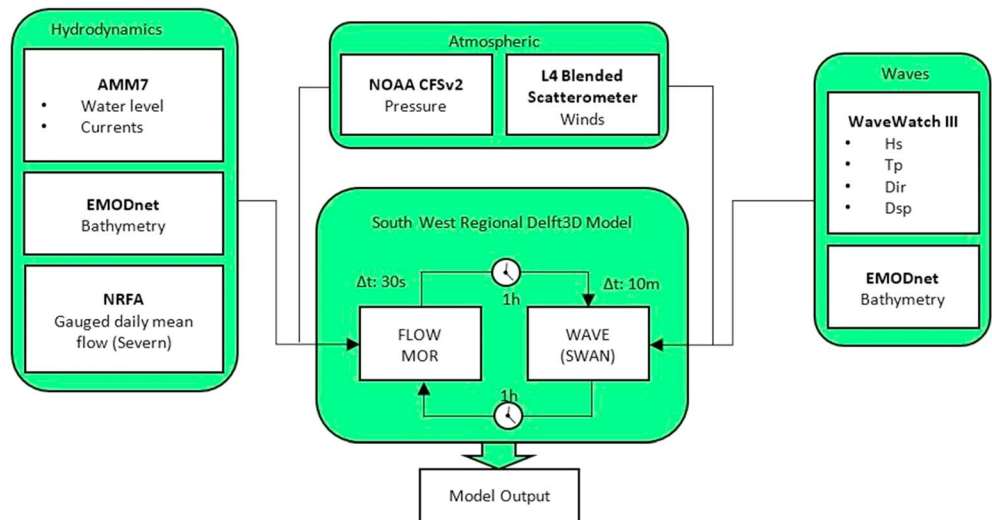
Figure 2. Model schematic diagram showing the integration of different modules and wave coupling.

This represents an eddy-permitting grid resolution, suitable to resolve mesoscale eddies at the length scale of the baroclinic Rossby radius (2–5 km on the shelf; Holt & Proctor, 2008), although eddies at the smaller end of this scale will not be fully resolved. Depths were averaged from 1/8° resolution EMODnet digital bathymetry (EMODnet Bathymetry Consortium, 2016), corrected to Mean Sea Level 2000 (MSL2000) using the Vertical Offshore Reference Frame (Turner et al., 2010).

The hydrodynamic model has four water level boundaries and one discharge boundary at the Severn. Water level data were interpolated at 7-km intervals across the boundaries from the Atlantic Margin Model (FOAM-AMM7; McConnell et al., 2017; O'Dea et al., 2012). Boundary conditions were then linearly interpolated between these 7-km intervals at the intermediate boundary nodes by the model. This interpolation can generate unrealistic flows adjacent to the open boundary. Consequently, data within 20 grid cells of each open boundary were excluded from the analysis. Boundaries were located far enough away from the South West peninsula in order that this did not influence the model results in the region of interest. Variations in the Severn discharge rate had little influence on modeled results; therefore, a representative average 100-m^3/s discharge was applied. The hydrodynamic time step was 30 s. Spatially variable winds were interpolated linearly from 0.25° resolution satellite scatterometer blended 6-hourly mean wind fields retrieved from the Copernicus Marine Service (Bentamy & Fillon, 2012). Spatially variable atmospheric pressure was interpolated linearly from the 0.5° resolution Climate Forecast System version 2 model (Saha et al., 2014).

The wave model overlapped the hydrodynamic domain at 1.5-km resolution. Depth and wind forcing were assigned in the same manner as the hydrodynamic model. The wave model was forced with parametric boundary conditions (H_s, T_p, direction, directional spreading) interpolated from the UK Met Office Wave Watch III continental shelf model (Saulter, 2017) at 8-km intervals along four open boundaries. The Severn boundary was closed. The wave domain extended slightly past the hydrodynamic domain in order to avoid hydrodynamic boundaries effects influencing the wave boundaries. The wave time step was 10 minutes. Waves were two-way coupled to the hydrodynamics with a 1-hr communication time step, passing wave forces based on energy dissipation rate or radiation stresses, bed shear stresses, Stokes drift, and orbital bottom velocity and receiving water levels, depth-averaged velocities, and updated bathymetry (Elias et al., 2012).

Bed-load and suspended-load sand transport rates were calculated using the TRANSPOR2004 formulation (van Rijn, 2007a, 2007b) with an essentially unlimited sediment depth for 330-μm grain size, similar to measured grain sizes along the North Coast and Bristol Channel (Channon & Hamilton, 1976; Lewis et al., 2015; Pattiaratchi & Collins, 1988; Prodger et al., 2017). A single grain size was important for comparisons of potential sand transport between regions with different hydrodynamic and morphological characteristics. In reality, grain size becomes progressively finer moving north through the Approaches. The Bristol Channel shows pronounced local variability with grain sizes ranging from mud and fine sand in low-

energy embayments to gravel and erosion-resistant substrate in high-energy locations (Channon & Hamilton, 1976; Collins, 1987; Pattiaratchi & Collins, 1988; Thompson et al., 2017; Ward et al., 2015).

3.2. Wave-Tide Interactions

Delft3D has been successfully used in a depth-averaged form in studies of wave-current interactions and sediment transport on the inner continental shelf (Hansen et al., 2013; Hopkins et al., 2015; Luijendijk et al., 2017; Ridderinkhof et al., 2016). Wave-current interactions are parameterized in the depth-averaged implementation of Delft3D. Wave-induced setup and long-shore currents, forced by wave-induced momentum flux due to radiation stress gradients, are approximated using the wave energy dissipation rate method of Dingemans et al. (1987). Wave-induced mass flux due to Stokes drift is represented as the integration of the Stoke's drift velocity components over the total wave-averaged water depth. SWAN accounts for depth and current-induced wave refraction, wave blocking by flow, and current-induced Doppler shift. The effect of a mean current on the wave energy dissipation due to bottom friction is not taken into account in SWAN due to large potential errors in estimating the bottom roughness length (Booij et al., 1999).

Enhancement of the bed shear stress under combined waves and currents is implemented in Delft3D following the method of Soulsby et al. (1993). The current-related bed shear stress τ_c is

$$\tau_c = \frac{g\rho_0 U|U|}{C_D^2} \tag{1}$$

and the wave-related bed shear stress is

$$|\tau_w| = \frac{1}{2}\rho_0 f_w U_{orb}^2 \tag{2}$$

where f_w is a wave-related friction factor, U_{orb} is the bottom orbital velocity, U is the depth-averaged velocity, ρ_0 is the density of seawater, g is the gravitational acceleration and C_D is the drag coefficient. The wave-related friction factor takes the form:

$$f_w = \begin{cases} 0.00251 \exp\left[5.21\left(\dfrac{U_{orb}}{\omega k_s}\right)^{-0.19}\right] & \text{for} \dfrac{U_{orb}}{\omega k_s} > \dfrac{\pi}{2}, \\[2em] 0.3 & \text{for} \dfrac{U_{orb}}{\omega k_s} \leq \dfrac{\pi}{2} \end{cases} \tag{3}$$

where ω is the apparent (Doppler-shifted) frequency, k_s is the Nikuradse roughness length, and the bottom orbital velocity is

$$U_{orb} = \frac{1}{4}\sqrt{\pi}\,\frac{H_{rms}\omega}{\sinh(kh)} \tag{4}$$

Time-mean bed shear stress τ_m and maximum bed shear stress τ_{max} are then determined using three dimensionless parameters X, Y, and Z:

$$X = \frac{\tau_c}{\tau_c + \tau_w}, \tag{5}$$

$$Y = \frac{\tau_m}{\tau_c + \tau_w}, \tag{6}$$

$$Z = \frac{\tau_{max}}{\tau_c + \tau_w}, \tag{7}$$

The parameters Y and Z are related to X by the following equations:

$$Y = X[1 + bX^p[1-X]^q] \tag{8}$$

$$Z = 1 + aX^m(1-X)^n \tag{9}$$

where a, b, p, q, m, and n are the coefficients fitted by Soulsby et al. (1993) to various wave-induced shear stress formulations, which are available in Delft3D and are chosen during calibration. The total bed shear stress is corrected for Stokes drift U^S:

$$\tau_b = \frac{|\tau_m|}{|U|}\left(U - U^S\right) \tag{10}$$

The TRANSPOR2004 sediment transport formulation (van Rijn, 2007a, 2007b) computes four sediment transport contributions: current- and wave-related suspended load and current- and wave-related bed load. The current-related suspended transport is the product of the depth-averaged concentration and current velocity, including the effects of wave stirring on the sediment load (van Rijn, 2007b). The reference concentration is calculated using the method of van Rijn et al. (2000) for a single sediment fraction:

$$c_a = f_{SUS}0.015\rho_s \frac{d_{50}(\tau_\alpha)^{1.5}}{a(D_*)^{0.3}} \tag{11}$$

where ρ_s is the sediment density, d_{50} is the median particle diameter, D_* is the dimensionless particle diameter, a is van Rijn's reference height, τ_α is the nondimensional bed-shear stress including the effects of currents and waves, and f_{SUS} is a user-defined tuning parameter set to 1.4 in accordance with Grunnet et al. (2004). The instantaneous bed load transport rate is

$$q_{b,t} = 0.5\rho_s d_{50}D_*^{-0.3}\left(\frac{\tau'_b}{\rho_0}\right)^{0.5}\left[\frac{\tau'_b - \tau_{b,cr}}{\tau_{b,cr}}\right] \tag{12}$$

in which τ'_b is the instantaneous grain-related bed shear stress due to combined currents and waves and $\tau_{b,cr}$ is the critical bed shear stress. The x and y components of the total bed load transport are then obtained by integrating the instantaneous bed load transport rate over the wave period T:

$$q_{b,x} = \left(\frac{1}{T}\right)\int \frac{v_b}{\left(u_b^2 + v_b^2\right)^{0.5}}q_{b,t}dt + q_{s,w}\cos(\phi) \tag{13}$$

$$q_{b,y} = \left(\frac{1}{T}\right)\int \frac{v_b}{\left(u_b^2 + v_b^2\right)^{0.5}}q_{b,t}dt + q_{s,w}\sin(\phi) \tag{14}$$

where u_b and v_b are the instantaneous near-bed velocity components due to the combined action of currents and waves and ϕ is the angle between the wave propagation direction and the x axis of the computational grid. The current-related bed load transport components are

$$q_{b,c,x} = \left(\frac{1}{T}\right)\int \frac{u_{b,c}}{\left(u_b^2 + v_b^2\right)^{0.5}}q_{b,t}dt \tag{15}$$

$$q_{b,c,y} = \left(\frac{1}{T}\right)\int \frac{v_{b,c}}{\left(u_b^2 + v_b^2\right)^{0.5}}q_{b,t}dt \tag{16}$$

where $u_{b,c}$ and $v_{b,c}$ are the instantaneous current-related velocity components. The wave-related bed load transport components are then determined from the difference between the total transport and the current-related transport:

$$q_{b,w,x} = q_{b,x} - q_{b,c,x} \tag{17}$$

$$q_{b,w,y} = q_{b,y} - q_{b,c,y} \tag{18}$$

An additional transport component is generated due to asymmetric wave orbital motion within about 0.5 m of the bed, which is included in the bed load transport vector. This wave-related suspended transport is modeled as

$$q_{s,w,x} = 0.1\left(\frac{U_{\delta,for}^4 - U_{\delta,back}^4}{U_{\delta,for}^3 + U_{\delta,back}^3} + u_\delta\right)L_T\cos(\phi) \tag{19}$$

$$q_{s,w,y} = 0.1\left(\frac{U_{\delta,for}^4 - U_{\delta,back}^4}{U_{\delta,for}^3 + U_{\delta,back}^3} + u_\delta\right)L_T\sin(\phi) \tag{20}$$

in which $U_{\delta,for}$ and $U_{\delta,back}$ are the forward and backward directed peak orbital velocities, u_δ is the wave-induced streaming velocity near the bed, and L_T is the approximated suspended sediment load. The final bed load transport components are the sum of the corrected current and wave related components:

$$Q_{b,x} = f_{BED}\left(q_{b,c,x}\right) + f_{BEDW}\left(q_{b,w,x}\right) + f_{SUSW}\left(q_{s,w,x}\right) \tag{21}$$

$$Q_{b,y} = f_{BED}\left(q_{b,c,y}\right) + f_{BEDW}\left(q_{b,w,y}\right) + f_{SUSW}\left(q_{s,w,y}\right) \tag{22}$$

where f_{BED}, f_{BEDW}, and f_{SUSW} are the tuning parameters set to 0.8, 0.3, and 0.3, respectively, in accordance with Grunnet et al. (2004) (see also McCarroll et al., 2018 ; van Rijn et al., 2004).

As this study considers depth-averaged computations, some effects of wave-current interactions are not represented. The effects of wave dissipation are applied in a depth-integrated manner, whereas for a 3-D simulation, wave breaking and whitecapping would be represented at the free-surface and bottom friction would apply at the bed layer. Additional turbulence production due to wave breaking and bottom friction is parameterized by inclusion in the horizontal eddy viscosity and diffusivity coefficients. The implications of this are discussed in section 5.

3.3. Calibration

Calibration was conducted over a 62-day simulation period from 1 December 2013 to 1 February 2014 for varying uniform bed roughness coefficients, dimensionless wind drag coefficient, and wave-induced bottom stress formulations. This covered the energetic winter 2013/2014 period that saw the strongest storms to affect the region in >50 years (Masselink et al., 2015, 2016; Scott et al., 2016). Model performance was assessed using an aggregation of skill metrics (R^2, bias, Willmott skill (d_r), Brier skill (bSkill), and mean absolute error (MAE) for residuals) against observed tide elevations, depth-averaged currents, and wave parameters from networks of tide gauges, ADCP deployments, and wave buoys (Figure 1). Qualitative sediment transport rates and directions were compared with previous observations, modeling results, and observed bed form asymmetries.

The skill metrics are outlined below. Bias is given by

$$BIAS = \frac{\sum_{i=1}^{n}(P_i - O_i)}{n} \tag{23}$$

where P_i is the ith model prediction, O_i is the ith observed value, and n is the number of points for comparison. Willmott skill d_r (Willmott et al., 2012) is given by

$$d_r = \begin{cases} 1 - \dfrac{\sum\limits_{i=1}^{n}|P_i - O_i|}{2\sum\limits_{i=1}^{n}\left|O_i - \overline{O}\right|}, \text{ when} \\[4pt] \sum\limits_{i=1}^{n}|P_i - O_i| \leq 2\sum_{i=1}^{n}\left|O_i - \overline{O}\right| \\[8pt] \dfrac{2\sum\limits_{i=1}^{n}\left|O_i - \overline{O}\right|}{\sum\limits_{i=1}^{n}|P_i - O_i|} - 1, \text{ when} \\[8pt] \sum\limits_{i=1}^{n}|P_i - O_i| > 2\sum\limits_{i=1}^{n}\left|O_i - \overline{O}\right| \end{cases} \tag{24}$$

where $\overline{P}$ and $\overline{O}$ are the predicted and observed mean, respectively. The score d_r ranges from −1 to 1 and indicates the summed magnitudes of the differences between the modeled and observed deviations about the observed mean, relative to the summed magnitudes for the perfect model, $P_i = O_i$ (Willmott et al., 2012).

Values >0 indicate that the sum of the error magnitudes is less than the magnitudes of the observed deviations (by half for $d_r = 0.5$).

Brier skill (BSS) is given in its decomposed form (Murphy & Epstein, 1989; Sutherland et al., 2004) by

$$BSS = \frac{\alpha - \beta - \gamma + \epsilon}{1 + \epsilon}, \text{where}$$

$$\alpha = r_{P'O'}{}^2, \quad \beta = \left(r_{P'O'} - \frac{\sigma_{P'}}{\sigma_{O'}}\right)^2, \quad \gamma = \left(\frac{\langle P'\rangle - \langle O'\rangle}{\sigma_{O'}}\right)^2, \quad \epsilon = \left(\frac{\langle O'\rangle}{\sigma_{O'}}\right)^2 \quad (25)$$

where P' and O' are the predictions and observations, σ denotes the standard deviation and $r_{P'O'}$ is the product moment correlation coefficient between the predictions and observations. Values of <0.3 are considered poor, 0.3–0.6 reasonable, 0.6–0.8 good, and >0.8 excellent.

Mean absolute error (Willmott & Matsuura, 2005) is given by

$$\text{MAE} = \frac{\sum_{i=1}^{n}(|P_i - O_i|)}{n} \quad (26)$$

Metrics were calculated for the unfiltered time series, and two residual time series calculated by methods described in Brown et al. (2012): harmonic analysis using U-Tide (Codiga, 2011) and low-pass filtering using a two-way recursive Chebyshev-II filter with passband ≥30 hr, stop band ≤26 hr, allowable passband ripple magnitude of 3 dB, and stop-band attenuation of 30 dB (allowing periods ≥30 hr to pass, attenuating periods ≤26 hr). The best performing calibration run was selected based on the run that scored best for the majority of the metrics considered. The default SWAN parameters and the Fredsøe (1984) bed shear stress formulation performed best, as used in studies of sediment dynamics in combined energetic tide and wave environments elsewhere (Herrling & Winter, 2018; Ridderinkhof et al., 2016; Verschelling et al., 2017). A minimum wind drag coefficient of 0.002 was selected. The Manning formulation for the drag coefficient was selected, which takes the form

$$C_D = \frac{\sqrt[6]{h}}{n} \quad (27)$$

where h is the total water depth. The calibrated roughness coefficient n was 0.0275. Section 3.4 presents the full validation, including the calibration period.

3.4. Model Performance
3.4.1. Water Levels
Validation was performed over a nine-month period from September 2013 to June 2014. Water levels were compared at hourly intervals using the nearest grid node to each gauge. The harmonic tide was subtracted from the total signal to give the harmonic residual elevation and a low-pass residual was determined through filtering, isolating long-period residual elevations and removing semidiurnal and diurnal signals. Two comparisons are shown in Figure 3: a representative site (Ilfracombe) and the worst performing site (Weymouth). Statistics for all sites are presented in Table 1.

Water levels were simulated with excellent skill across the domain at all gauges apart from Weymouth (G8; Figure 1). The model did not simulate the double-low water at Weymouth due to the proximity of this gauge to the boundary and because the model domain does not encompass the degenerate amphidromic system to the east. Despite this, high water was simulated well, as shown in the scatterplot (Figure 3, right). Bias in the low-pass residuals reflects the water level bias, tending toward slight underestimation with an overall bias of −13 cm. MAE (not shown for unfiltered signals) is 20 cm overall, reflected in the harmonic residual (19 cm).

3.4.2. Currents
Two ADCP deployments at the WaveHub on the North Coast were used for validation (WHE, WHW; Figure 1; Lopez et al., 2016). Instantaneous velocity profiles were despiked by the method of Mori et al. (2007), depth-integrated and hourly averaged for comparison. Model data were linearly interpolated to the ADCP locations. Comparison was conducted for periods of continuous ADCP data and gaps were not
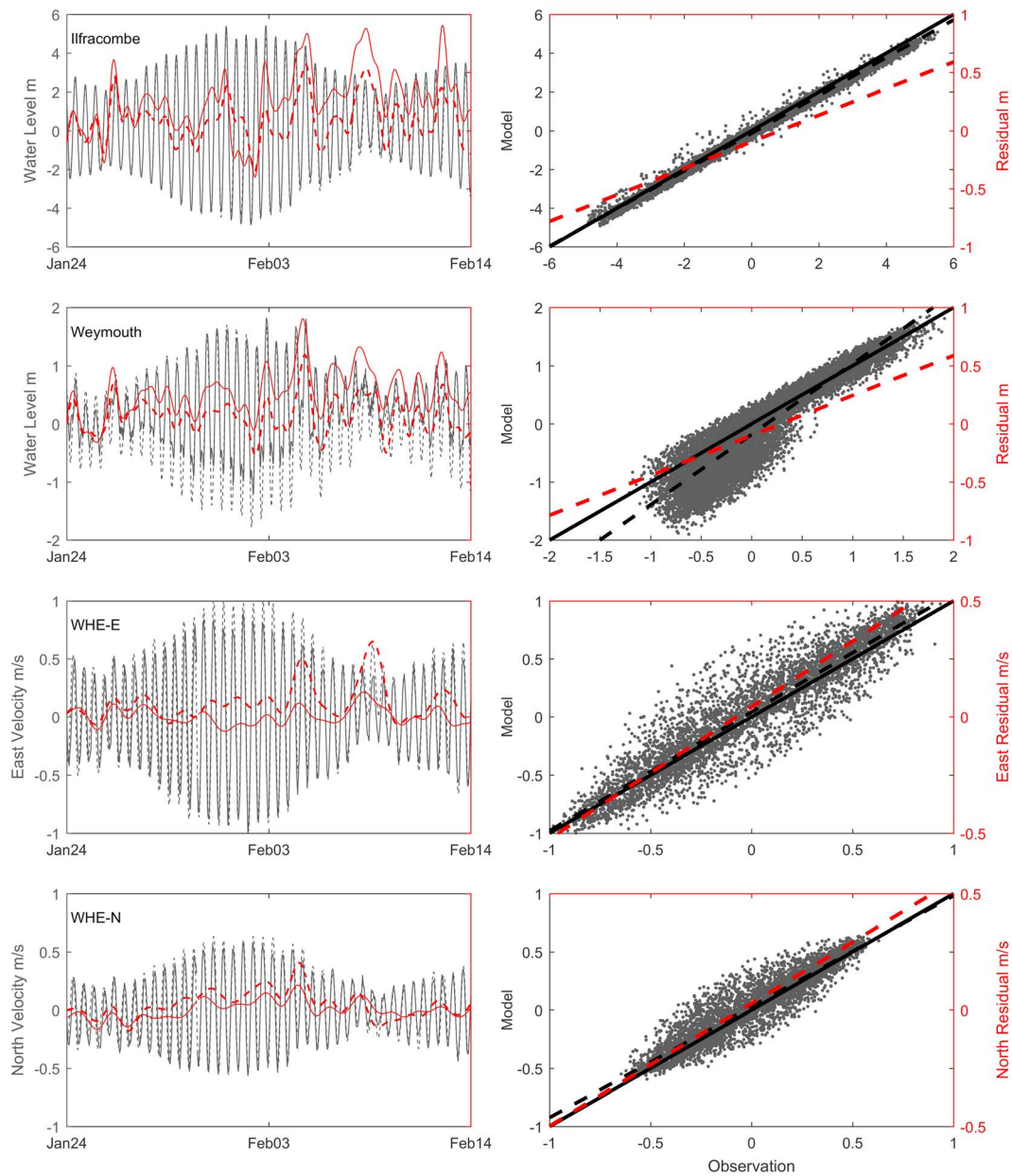
Figure 3. Model (dashed) versus observation (solid) comparisons for water levels (top half) and depth-averaged velocities (bottom half) for a period of energetic storms. The tidal signal (grey) and residual signal (red) are shown, with residuals presented from the low-pass filtering method only to reduce complexity. Velocities from the Wave Hub East deployment are presented, separated into east and north components. Scatter plots (right column) show the modeled parameters versus the observations for the full nine-month data set. The 1:1 line of the perfect model (solid) and the trend line of the modeled parameters versus the observations (dashed) are shown for the tidal (grey) and residual (red) signals.

filled. Comparisons are shown for the tidal and residual signals in the same manner as water levels in Figure 3.

Currents were simulated with good skill at both deployments (Table 1) with an eastward bias of 3 cm/s and northward bias of 2 cm/s, and MAE (not shown) of 9 and 5 cm/s, respectively, reflected in the residual currents by low-pass filtering (bias) and harmonic analysis (MAE). WHW predictions have greater spread about the perfect model than WHE, reflected in a lower R^2. Depth-averaged residuals tend toward overestimation by several centimeters per second, greater during storm events. Considering that ADCP measurements closer to the surface than 10% of the water depth cannot be used due to sidelobe contamination (Marmorino & Hallock, 2001), this result is considered very good.

Table 1
Model Validation Statistics for Tidal Elevations, Currents, and Waves, Including Residuals From Two Filtering Methods

	Water levels (m)											
	Unfiltered signal				Low-pass residual				Harmonic residual			
Location	N	R^2	BIAS	d_r	bSkill	R^2	BIAS	d_r	MAE	R^2	BIAS	d_r	MAE
G1	13104	0.99	−0.18	0.94	**0.99**	0.80	−0.18	0.46	0.18	0.35	−0.04	0.57	0.17
G2	13104	0.99	−0.02	0.96	**0.99**	0.81	−0.02	0.76	0.09	0.57	−0.06	0.67	0.23
G3	13104	0.995	−0.12	0.96	**0.99**	0.78	−0.12	0.61	0.13	0.27	−0.04	0.56	0.26
G4	13104	0.996	−0.13	0.96	**0.99**	0.74	−0.13	0.58	0.14	0.32	−0.03	0.58	0.20
G5	13104	0.99	−0.17	0.92	**0.97**	0.51	−0.17	0.34	0.18	0.38	0.00	0.56	0.13
G6	13104	0.99	−0.12	0.94	**0.98**	0.69	−0.12	0.53	0.13	0.38	−0.02	0.58	0.13
G7	13104	0.99	−0.16	0.91	**0.96**	0.71	−0.16	0.45	0.16	0.50	−0.03	0.61	0.13
G8	13104	0.86	−0.14	0.75	<u>0.22</u>	0.71	−0.14	0.47	0.15	0.16	−0.01	0.11	0.24
ALL	104832	0.99	−0.13	0.94	**0.99**	0.68	−0.13	0.54	0.15	0.31	−0.03	0.56	0.19

	Currents (m/s)											
	Unfiltered signal					Low-pass residual				Harmonic residual			
Location	N	R^2	BIAS	d_r	bSkill	R^2	BIAS	d_r	MAE	R^2	BIAS	d_r	MAE
WHE-E	2811	0.95	0.03	0.89	**0.85**	0.53	0.03	0.09	0.04	0.28	0.01	0.46	0.04
WHE-N	2811	0.93	0.01	0.87	**0.60**	0.43	0.01	0.18	0.01	0.30	0.01	0.53	0.02
WHW-E	5794	0.86	0.03	0.82	**0.74**	0.51	0.03	0.12	0.03	0.03	0.002	0.50	0.11
WHW-N	5794	0.86	0.02	0.83	**0.72**	0.49	0.02	0.17	0.03	0.05	0.004	0.51	0.07
ALL-E	8605	0.88	0.03	0.84	**0.76**	0.53	0.03	0.22	0.03	0.04	0.002	0.50	0.09
ALL-N	8605	0.86	0.02	0.84	**0.68**	0.46	0.02	0.17	0.02	0.06	0.005	0.51	0.05

	Waves											
	H_s (m)					T_P ($H_s > 1$ m) (s)				Dir ($H_s > 1$ m) (°)			
Location	N	R^2	BIAS	d_r	bSkill	N	R^2	BIAS	d_r	bSkill	R^2	BIAS	d_r	bSkill
B1	6553	0.74	0.11	0.68	**0.96**	856	0.17	−0.25	0.04	<u>−2.86</u>	0.73	5.99	0.74	**0.72**
B2	6553	0.87	0.15	0.80	**0.93**	3799	0.53	0.11	0.64	**0.83**	0.14	0.80	0.52	**0.69**
B3	6553	0.92	0.12	0.88	**0.97**	4285	0.68	−0.29	0.74	**0.89**	0.38	14.10	0.28	**0.73**
B4	6553	0.87	0.42	0.65	**0.68**	2055	0.28	2.98	0.31	*0.54*	0.16	−7.84	−0.06	*0.58*
B5	6553	0.82	0.39	0.78	**0.73**	3333	0.36	0.82	0.58	**0.71**	0.18	−5.64	0.49	*0.59*
B6	6553	0.89	0.28	0.77	**0.90**	3041	0.29	2.37	0.45	*0.47*	0.30	−12.70	0.22	*0.55*
B7	6553	0.80	0.32	0.66	**0.80**	2000	0.36	1.31	0.51	<u>0.14</u>	0.64	−17.25	0.53	**0.62**
B8	6553	0.62	0.17	0.66	**0.75**	373	0.20	0.23	0.09	<u>−1.11</u>	0.33	−9.02	0.57	<u>0.29</u>
B9	6553	0.79	0.24	0.66	**0.83**	1201	0.25	1.40	0.41	<u>−0.19</u>	0.53	−3.14	0.66	**0.60**
B10	6553	0.88	0.11	0.83	**0.95**	2870	0.32	1.30	0.57	*0.30*	0.31	−5.82	0.41	**0.69**
B11	6553	0.87	0.13	0.83	**0.94**	3174	0.32	1.39	0.58	*0.34*	0.27	−4.90	0.76	**0.92**
B12	6553	0.78	0.28	0.62	**0.62**	963	0.21	2.43	0.30	<u>0.11</u>	0.40	−4.52	0.54	*0.54*
ALL	78636	0.86	0.23	0.78	**0.90**	27950	0.38	1.07	0.62	*0.53*	0.91	−2.98	0.85	**0.84**

Note. Brier skill scores are coded for excellent and good (bold), reasonable (italic), and poor (underlined) model skill. For residual water elevations and depth-averaged currents, the mean absolute error is presented instead of Brier skill.

3.4.3. Waves

Comparisons of wave parameters for Bideford (B2) and Start Bay (B7) are presented in Figure 4 with statistics presented in Table 1. Bideford is representative of performance at exposed sites such as the North Coast (B2-3), Chesil (B10-11), and Looe Bay (B6). Exposed sites show excellent skill when compared to the buoy data for H_s. Start Bay is representative of sites with smaller wave heights due to sheltering. The model captures the bimodal (southerly/easterly) wave climate. Considerable scatter in observed wave directions is apparent for $H_s < 1$ m (light blue) where buoy measurements are less reliable. Eliminating times where $H_s < 1$ m improves model skill for direction. Locations with a majority $H_s < 1$ m tended to be sheltered due to the shape of the coastline (e.g., B7: Start Bay, B8: Tor Bay; Figure 1), or the presence of features such as islands (e.g., B6: Looe Bay; Figure 1). The model tends to overpredict H_s in sheltered locations when the 1.5-km resolution cannot resolve small-scale coastal features. In these locations, sheltering features such as
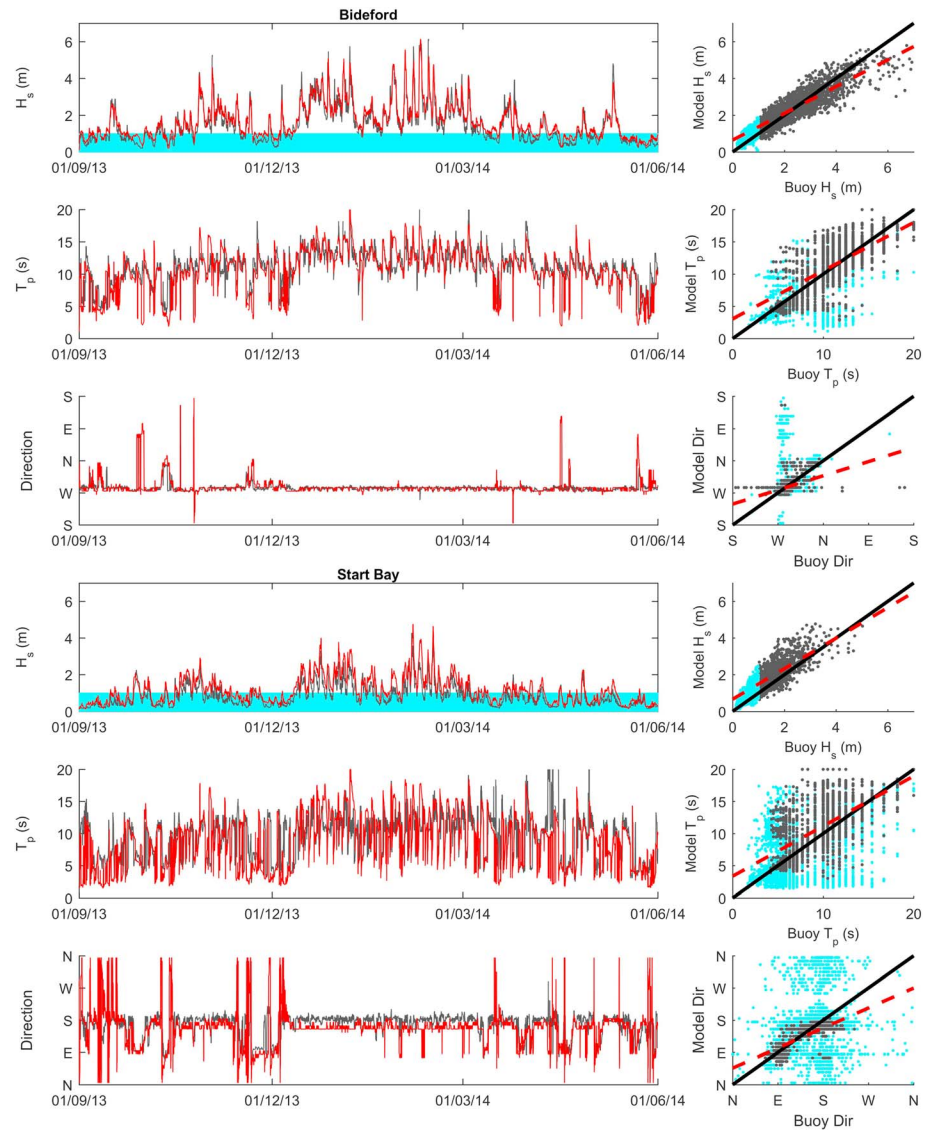
Figure 4. Model (red) versus observation (grey) comparisons for wave parameters at Bideford and Start Bay for the full nine-month validation period. The region for $H_s < 1$ m is shaded blue. The *x-y* plots on the right show the modeled versus the observed wave parameters. Data where the observed significant wave height was <1 m are shaded blue. Observation time series have been median filtered over 6 hr for clarity due to considerable scatter in the wave buoy observations; however, validation and the *x-y* plots were performed on the unfiltered data. The 1:1 line of the perfect model and the trend line of the modeled parameters versus the observations are shown. The trend line excludes data where the observed H_s was <1 m.

headlands, islands, and sand banks that affect the wave climate at the buoy may not be well resolved. These effects are localized close to shore, and as this study is interested in regional-scale sand transport patterns, are not expected to impact the results. The model simulates H_s and direction with excellent skill overall, and T_p with reasonable skill. Overall biases are 23 cm, 1.1 s, and −3° for H_s, T_p ($H_s > 1$ m), and direction ($H_s > 1$ m), respectively, with MAE (not shown) of 30 cm, 2.2 s, and 11.7°.

The majority of Brier scores (47/54) indicate reasonable or better performance (and 38/54 indicate good or excellent). Areas with poor skill are explained by either proximity to the model boundary and highly site-specific tidal characteristics (Weymouth), or a lower number of wave observations for $H_s > 1$ m for comparison. This testifies to the suitability of this model for reproducing the wave and tidal characteristics of this region.
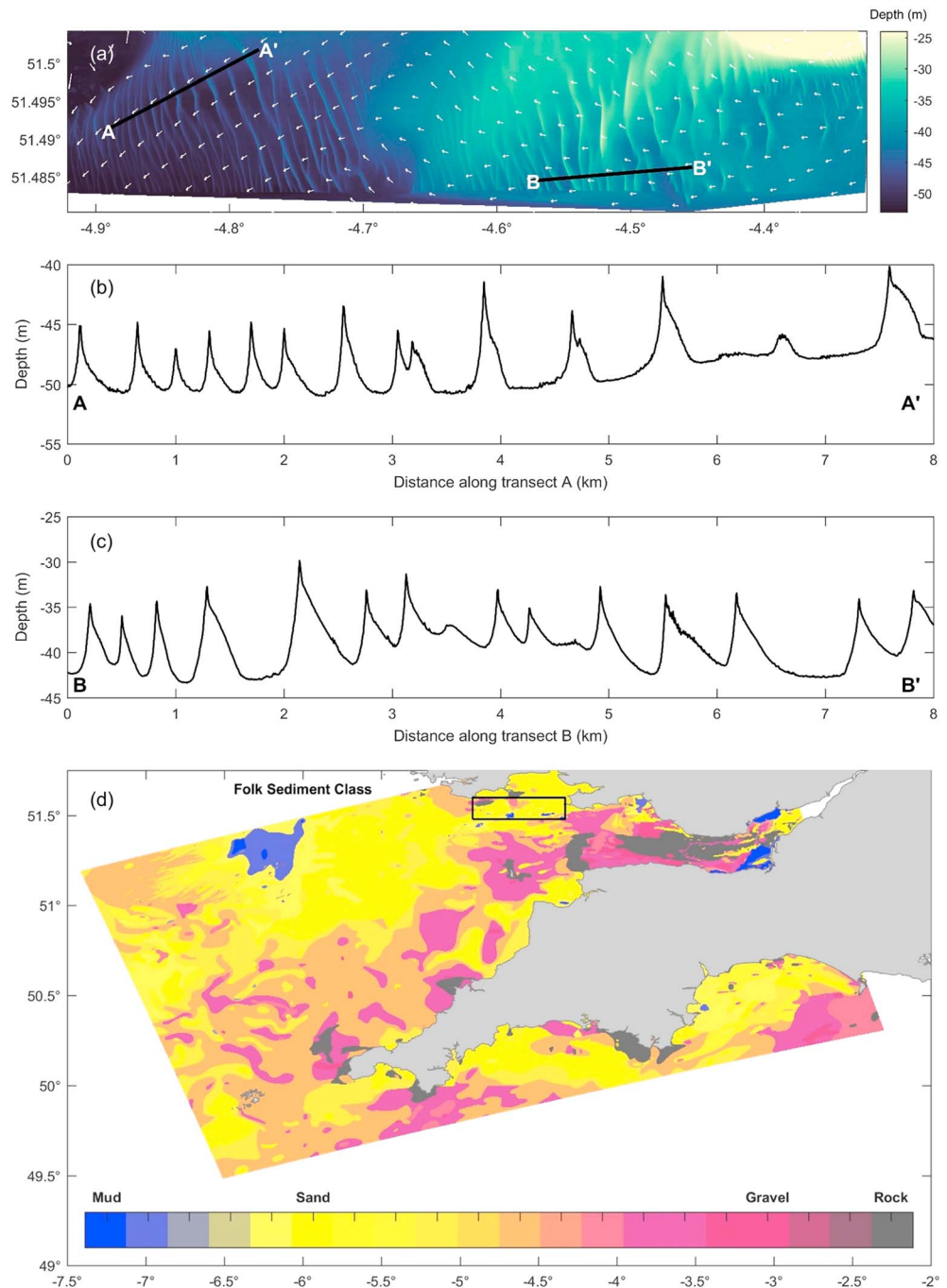
Figure 5. (a–c) Observed sandwaves from UK Civil Hydrography Programme single-beam bathymetry (UKHO). Predicted spring tide bed load transport vectors indicate direction only. Transects show sandwave asymmetry indicating bed form migration aligned with the model prediction. (d) Folk sediment class (Folk, 1954) obtained from British Geological Survey product DiGSBS250K. All classes are included, broadly grouped into mud, sand, gravel, or rock.

3.4.4. Sand Transport

Tide-only bed load transport vectors were compared with observed sandwaves from UKHO single-beam bathymetry south of Carmarthen Bay (Figure 5). Depths along two transects bisecting the sandwaves were extracted, referenced to mean sea level (MSL2000). Sandwave asymmetry is a common indicator of sand-wave migration in the direction of the steeper face (Knaapen, 2005). Observed sandwave asymmetry (Figures 5b and 5c) and crest orientation qualitatively match predicted spring tide bed load transport

vectors, suggesting that migration of these waves is controlled by spring tide hydrodynamics. Sand transport magnitude and direction south of the Gower during extreme westerly waves at neaps (~45 g·cm^{-1}·s^{-1} to the northeast) matches bed load transport rates calculated under similar conditions by Pattiaratchi and Collins (1988) (48 g·cm^{-1}·s^{-1} to the northeast) from near-bed current meter data. These observations lend confidence to model predictions of potential sand transport, offering a means of validating modeled sand transport in the absence of direct measurements.

Model sensitivity to peak period was tested over extreme waves at springs (details of simulated scenarios are given in section 3.5 and Figure S1). The magnitude of the peak period was varied by the model bias (± 1.1 s). Across most of the domain, this resulted in a reduction of sand transport rates within 20% of the tested reference scenario, and was unlikely to impact the qualitative results presented in this paper (Figure S2).

This study considers potential transport with a homogeneous medium sand bed. The sediment Folk classification for this region is shown in Figure 5d, from the British Geological Survey product DiGSBS250K, with sand classes shown in shades of yellow (Folk, R. L., 1954). Much of this region is composed of sand or gravelly sand. A comparison between modeled sand transport results from the simulated scenarios and observed grain sizes is discussed in section 5.

3.5. Simulated Scenarios

The interdependent relationship between marginal probability distributions of offshore H_s and T_p from four years of WWIII data (2013–2016) on the most south-western and deepest extent of the domain boundary was modeled following a copula approach outlined in Genest et al. (2007). H_s and T_p were, respectively, fitted with generalized extreme value and Rician marginal distributions (the best fitting distributions using the Akaike information criterion), with their joint-probability distribution described by a Gumbel copula (Figures S1a and S1b).

An extreme (1% exceedance) offshore H_s of 9 m is predicted, corresponding to a nearshore H_s of ~6 m on the North Coast, matching observed extreme wave heights reported in Scott et al. (2016) of 5.9 m at Sevenstones (off Land's End). Two joint-probability $H_s \cap T_p$ exceedance conditions were selected: median $H_s \cap T_{p50\%}$ (2 m, 10.5 s) and extreme $H_s \cap T_{p1\%}$ (9 m, 18 s). Two directions were selected from the modal wave directions at the same location (Figure S1c), west (270°) and west-northwest (292.5°), resulting in four simulated wave conditions (Figure S1d). Wind was not included; therefore, only swell was simulated. Peak orbital velocities in the region are induced by swell waves (Draper, 1967).

Simulations were performed over a full spring-neap tidal cycle with seven days of model spin-up time. Tidal forcing was generated by subtracting the harmonic residual elevation at each boundary node, leaving only the astronomic tide for a period of a full 14.72-day spring-neap cycle (31 January to 16 February 2014). Four consecutive spring tides and four consecutive neap tides were extracted from the cycle and averaged for analysis (Figure S1e).

Additionally, a tide-only simulation and wave-only simulation were performed. The wave-only simulation was coupled to the hydrodynamic module without any hydrodynamic forcing at the open boundaries, to simulate the individual effect of waves on sand transport in the absence of tidal currents, and therefore quantify the purely wave-driven sand transport component. These were then used to determine the contribution of nonlinear wave-current interactions.

4. Results

Depth-averaged velocity was integrated over springs, neaps, and a full spring-neap cycle for the tide-only simulation (Figure 6). The residual (mean) current distribution qualitatively matches results published elsewhere (Bricheno et al., 2015; Holt et al., 2001; Pingree & Griffiths, 1980; Uncles, 1982, 2010). The South Coast exhibits an ebb-dominated residual broadly to the southwest, flood and ebb dominance being defined by the half of the tidal cycle contributing most to the residual. The North Coast has a progressively weakening north-eastward residual, interrupted by large headland-enclosed embayments. Large embayments exhibit residual flow into the embayment with return flow at the sides, for example Carmarthen Bay, St. Ives Bay, and Bideford Bay. An ~10-cm/s ebb-dominated residual flows through St. George's Channel to the southwest before rotating west out of the domain. The Bristol Channel's deep
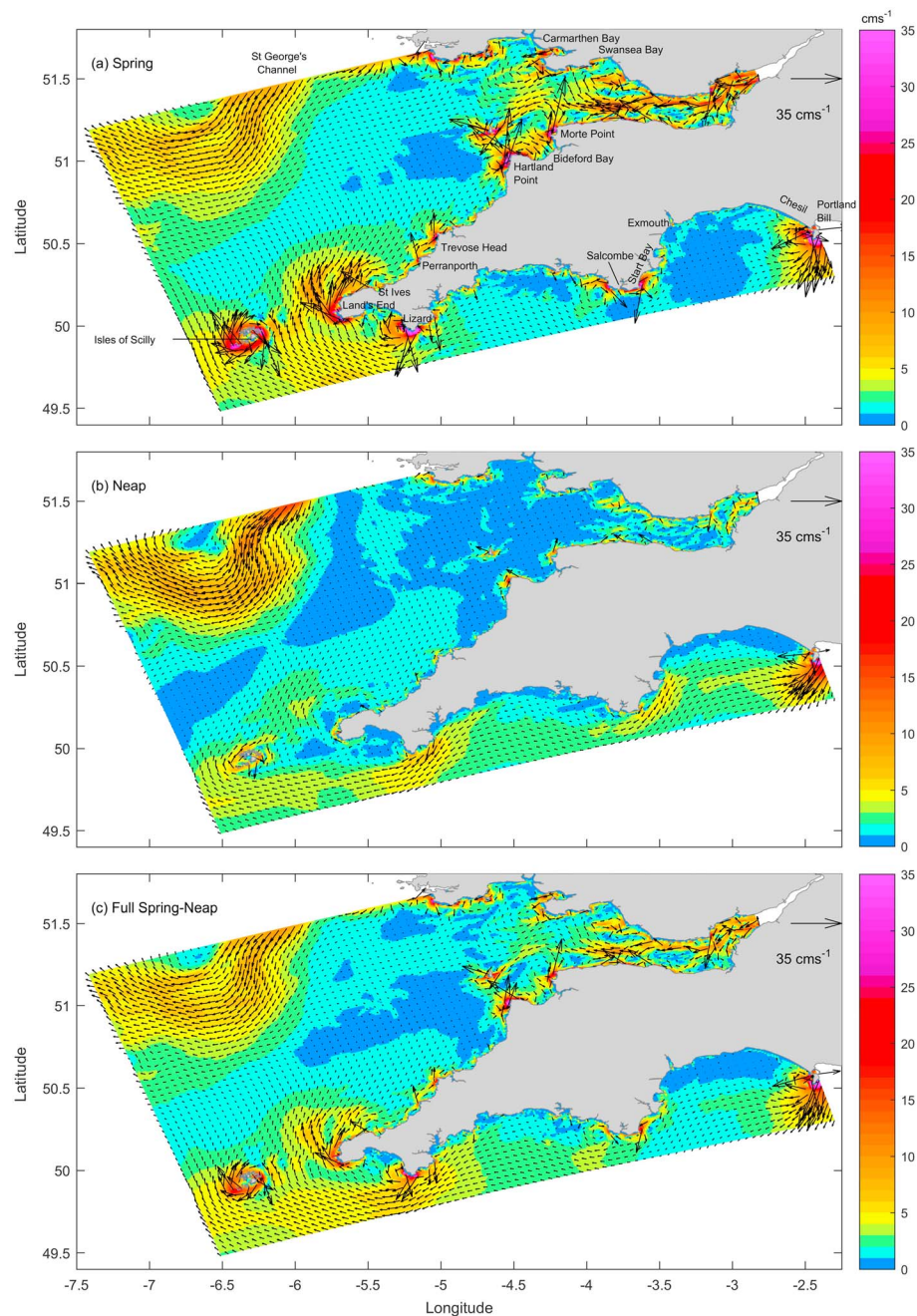
Figure 6. Mean current over (a) spring tides, (b) neap tides, and (c) a full spring-neap tidal cycle. Vectors are shown every 4 km for clarity. Values are presented in cm/s.

central channel is ebb-dominated, with residual westward flow. The spring-neap residual (Figure 6c) is dominated by the spring tide signal (Figure 6a) over the North Coast, Bristol Channel, and Approaches; however, for the South Coast it is dominated by a stronger ebb-dominant neap signal (Figure 6b). The Isles of Scilly interrupt the residual around the tip of the South West Peninsula with a strong (approximately 20 cm/s) clockwise circulation around the archipelago resulting from a flood-dominant north and ebb-dominant south shore.

Headland-associated eddies are present west of Portland Bill, Salcombe, and The Lizard with smaller eddies present in the lee of smaller headlands (e.g., along the North Coast). The clockwise spring-tide eddy west of
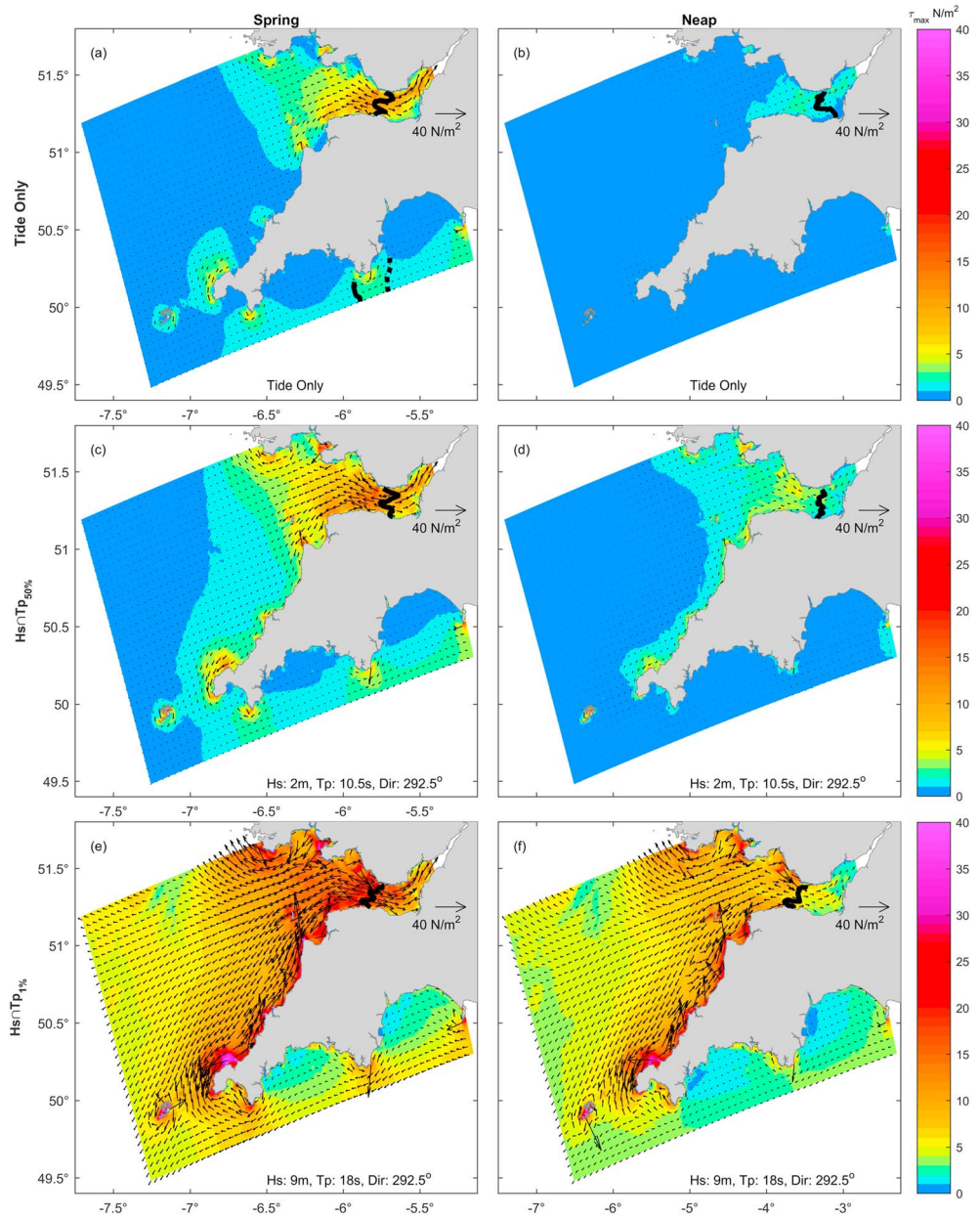
Figure 7. Maximum bed shear stress over a (left) spring and (right) neap tidal cycle for the (top) tide-only, (middle) 50% exceedance, and (bottom) 1% exceedance wave condition. Vectors are shown every 6 km for clarity. Solid black lines indicate the Bristol Channel and South Coast partings; the dashed line indicates a South Coast convergence zone. Wave conditions are annotated at the bottom of each plot.

Portland Bill drives a south-eastward coastal residual past Chesil. Residual eddies at the margins of the Bristol Channel are associated with linear sandbanks, such as Scarweather Sands south of Swansea Bay. The largest-magnitude residuals are off headlands at Hartland Point, Trevose Head, Perranporth, Start Point, Lizard Point, Portland Bill, and Morte Point. During springs, a divergence emerges south of Salcombe, and a convergence south of Exmouth. The intervening region is flood-dominant during springs and ebb dominant at neaps. Coastal residuals are largest during springs.

Strong spring-neap differences are present in tidal bed shear stress (Figures 7a and 7b) with spring values up to 15 N/m^2 in the Bristol Channel and off headlands, and values at neaps less than 1 N/m^2 across the domain apart from the Bristol Channel (up to 3 N/m^2). Tides exert a greater relative influence on bed shear stress in

the Bristol Channel than the Approaches. Tidal bed shear stress is greater in regions of strong topographic curvature, such as large promontories where tidal currents are greatest.

Results are shown for WNW waves (292.5°). During median waves ($H_s \cap T_{p50\%}$; Figures 7c and 7d), bed shear stress increases by a factor of 2 across much of the domain, with similar spatial distribution to tidal bed shear stress. Maximum bed shear stress over a tidal cycle during extreme conditions ($H_s \cap T_{p1\%}$; Figures 7e and 7f) increases by over an order of magnitude versus tide-only maximum stress along the North Coast and Approaches, and a factor of 3 in the Bristol Channel. The greatest bed shear stresses are off headlands, with magnitudes >40 N/m^2 at North Coast headlands during extreme forcing. Changing wave direction between WNW and west had little effect on the bed shear stress distribution.

The position of the Bristol Channel shear stress parting is sensitive to incident wave climate and tidal state. The divergence is seen between Porlock and Nash Point at springs for tide-only forcing (Figure 7a). At neaps, the tidal divergence shifts up channel to a (less distinct) line between Barry and Bridgewater Bay (Figure 7b). Median waves (Figures 7c and 7d) shift the whole divergence slightly eastward at springs, and the southern part westward at neaps. Extreme waves shift the bed load parting westward to a line west of Porlock, unaffected by tide state (Figures 7e and 7f). A weak tidal divergence extends south of Salcombe (South Coast) during springs, with convergence south of Exmouth. These are not present during neaps or under wave forcing.

Sand transport maps (Figure 8) show net sand transport per tidal cycle for tide-only and coupled wave + tide conditions for WNW waves. Both wave directions simulated result in similar spatial distributions of sand transport, although a slightly greater magnitude is predicted in the Bristol Channel and South Coast for westerly waves with notably greater wave influence in embayments of the northern Bristol Channel.

Significant tide-only net sand transport (Figures 8a and 8b) is isolated to spring tides and areas of the strongest tidal currents, such as the Bristol Channel and around large promontories at neaps. The North Coast has northeast net sand transport during springs, rotating anticlockwise and decreasing in magnitude moving offshore into the Approaches. The Bristol Channel has a bed load parting near Porlock with large potential net sand transports adjacent to the divergence directed up (down) channel to the east (west) of the divergence, interrupted by local deviations into the center of large embayments. Other locations with large transport magnitudes are off headlands with low magnitudes in embayments. Transport vectors are directed east into the sand-rich Loughor Estuary on the east side of Carmarthen Bay. A divergence is present south of Salcombe, with a convergence south of Exmouth, matching maximum bed shear stress vectors. The Isles of Scilly has a clockwise tide-only sand transport circulation around the archipelago.

The superposition of median waves ($H_s \cap T_{p50\%}$; Figures 8c and 8d) results in similar spatial patterns of sand transport to tides alone, generally enhancing tidal sand transport in shallow water with little influence in deeper areas where the waves have a smaller effect on the bed. The North Coast net northeast sand transport is disrupted, shifting counterclockwise toward the offshore with greater magnitude closer to shore. Sand transport in the Bristol Channel embayments increases by an order of magnitude. Net sand transport is directed out of Carmarthen Bay, indicating a direction shift versus the low-magnitude tide-only case. Sheltering of the South Coast from westerly and WNW waves by large promontories (Lizard Point, Start Point) combined with a lower tidal range results in distinct regions of minimal tidal and wave forced sand transport within the large-scale south facing embayments (e.g., Lyme Bay).

Extreme superimposed waves ($H_s \cap T_{p1\%}$; Figures 8e and 8f) increase sand transport by an order of magnitude across the Approaches at springs, with greater impact closer to shore. These waves mobilize medium sand at all depths across the domain. The exposed North Coast is impacted most, where tidally immobile sands in shallow water embayments are fully exposed to the incident waves and net sand transport increases by a factor of >100 out to 60-m depth in areas where tidal net sand transport is low. This indicates the potential for widespread mobilization of tidally immobile sand deposits during high-energy wave events. Within the Bristol Channel, the impact of waves on sand transport is significantly smaller, as waves propagating up-channel are attenuated due to bottom friction. Although the South Coast is relatively protected from west/WNW waves, increases in transport magnitude of factor ~25 are extensive offshore, decreasing to the east.
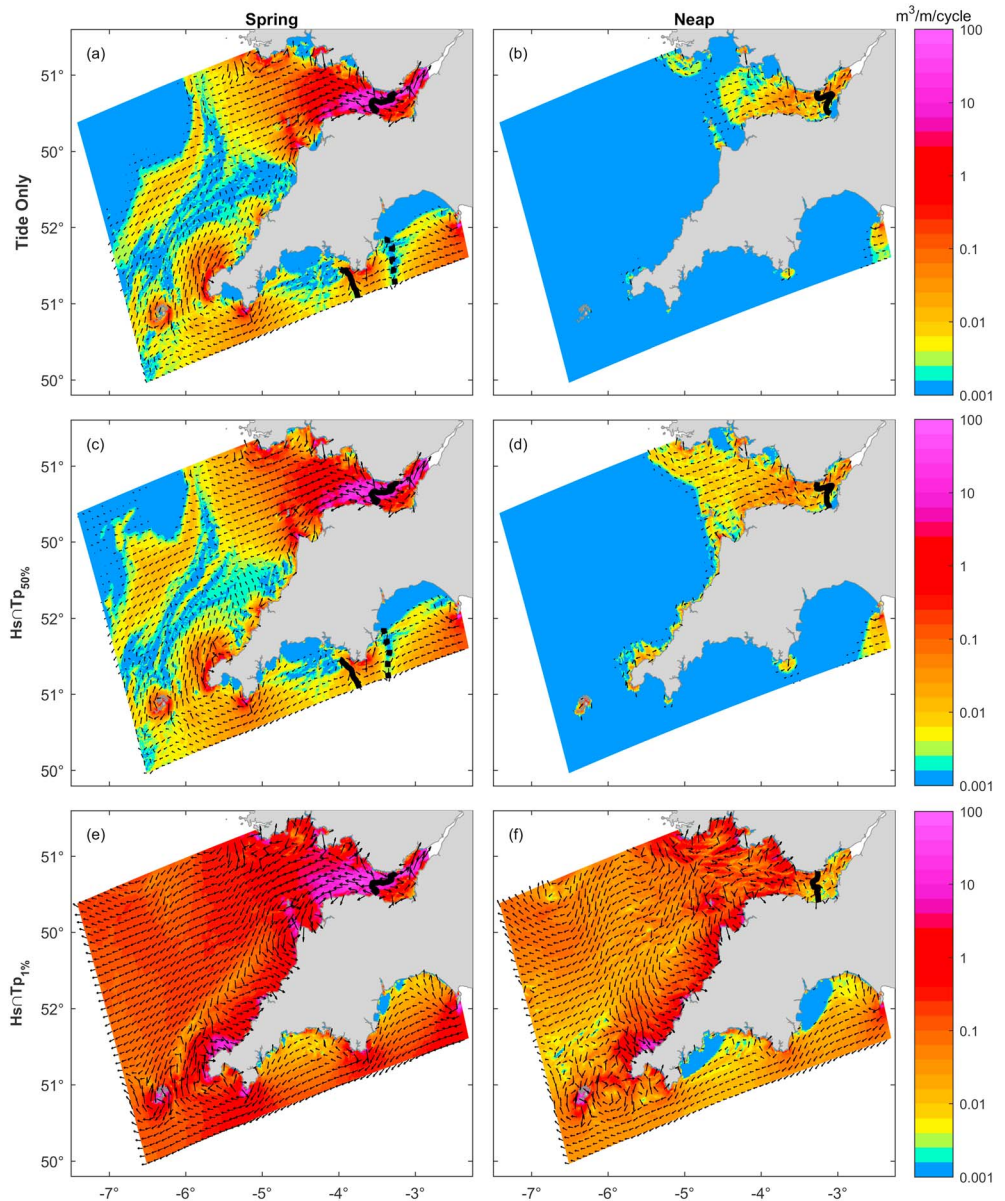
Figure 8. Cumulative sand transport for spring and neap tides and tide-only, median ($H_s \cap T_{p50\%}$), and extreme ($H_s \cap T_{p1\%}$) forcing conditions. Sand transport was averaged over four consecutive spring/neap tidal cycles. Values below 0.00016 m^3 m cycle have been removed based on the lower transport rates presented in the transport formulation validation in van Rijn (2007b). Vectors have been thinned to 6 km for clarity. The Bristol Channel and South Coast sand transport partings are shown with black lines. The dashed line represents an area of convergent sand transport.

To highlight the relative influence of waves, tides, and wave-tide interactions on sand transport magnitude, bar graphs of net sand transport per tidal cycle spatially averaged over 5-m depth bins are presented (Figure 9). The domain was split into the Approaches, Bristol Channel, and South Coast to highlight the effect of different hydrodynamic regimes and wave exposures (macrotidal versus mesotidal; exposed versus sheltered). The Isles of Scilly were excluded from the Approaches due to their distinct sand transport regime around the archipelago, which dominated the shallowest depth bins (0–15 m).

In the Approaches (Figures 9a and 9b), net sand transport during extreme waves increases by an order of magnitude versus tides alone, and all depths are activated, with sand transport occurring in regions of negligible tidal sand transport. Tide-only sand transport switches off during neaps across the Approaches and little sand transport occurs during median waves at neaps, isolated to the shallowest bins. In the Bristol
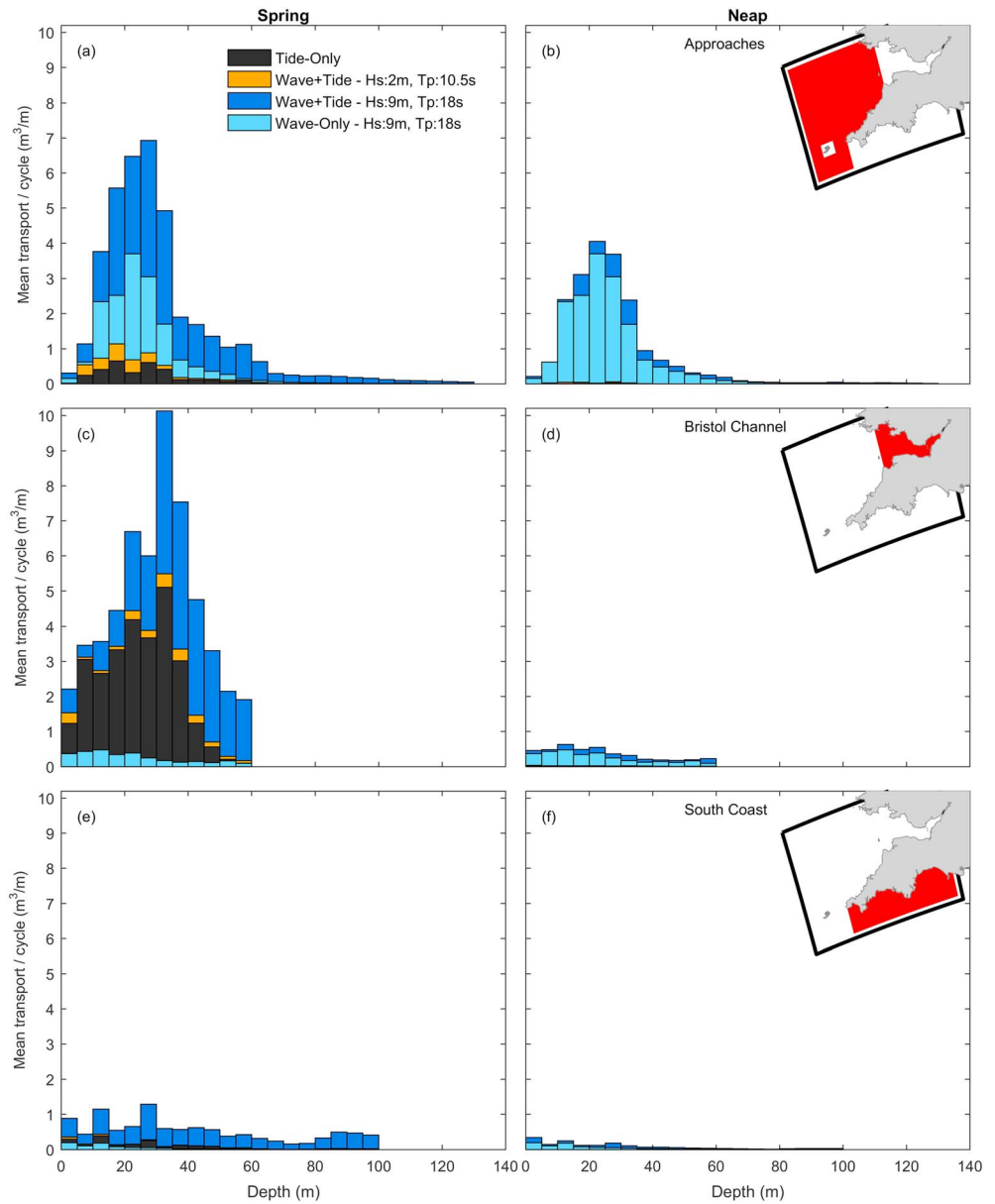
Figure 9. Sand transport integrated over 5-m depth bands for the (a and b) Approaches, (c and d) Bristol Channel, and (e and f) South Coast, for tide-only, wave-only, and wave + tide conditions. Heights of the bars represent the spatial mean sand transport magnitude per tidal cycle over that depth band. The wave conditions shown are for WNW waves (292.5°). Wave direction had a small effect on the magnitude; however, the distribution remained the same for Westerly and WNW waves.

Channel (Figures 9c and 9d) tides dominate net sand transport during springs <30-m depth for all conditions. Median waves have little relative effect at all depths. In deeper waters near the channel mouth, waves dominate net sand transport during high-energy conditions as tide-only sand transport diminishes. Similar to the Approaches, tidal net sand transport in the Bristol Channel is very low during neaps, and waves dominate during high-energy conditions.

The South Coast is relatively sheltered from waves from the west/west-northwest, resulting in relatively low wave-forced sand transport magnitudes, especially in the lee of large promontories such as Start Point and Lizard Point (Figure 8). Westerly/WNW wave forcing at the south and east boundaries is atypical for the South Coast (e.g., see the bimodal wave climate at Start Bay; Figure 4). Further consideration of Southerly

and Easterly wave events would be beneficial when considering wave impacts on sand transport along this coastline. Refraction of westerly/WNW waves results in sand transport across all depths and exposure of the east side of large embayments to wave forcing (e.g., Lizard Point-Start Point/Lyme Bay), with sheltering of the west side. Peaks at 10–15 and 25–30 m result from enhanced sand transport off Lizard Point, Start Point, and Portland Bill. Note that these are spatial averages, and considerable local variability was observed (Figure 8); however, they serve to highlight and quantify the broad spatial trends in net sand transport.

Wave-only net sand transport is shown for extreme WNW waves (light blue bars; Figure 9). Tide-only (dark grey) and wave-only transport are not equal to coupled wave + tide transport (dark blue). In the Bristol Channel, tides exert a greater influence than waves on sand transport and stronger tidal currents are able to transport wave-mobilized sand, despite low wave-only transport magnitudes. The nonlinear effect of waves + tides accounts for a significant proportion of net sand transport during extreme conditions, dominating sand transport in the deep central channel where wave-only and tide-only transport magnitudes are low. Waves exert a greater influence than tides on the exposed North Coast during extreme conditions. During median conditions, tide- and wave-driven sand transports have similar magnitude. Nonlinear interactions are dominant for depths >30 m. At neaps, waves dominate sand transport with significant sand transport occurring only in shallow water for median waves, negligible tide-only sand transport, and smaller contributions from nonlinear wave-tide interactions.

5. Discussion

This paper has presented residual tidal circulation, maximum bed shear stress, and sand transport rates for extreme and median wave conditions and spring and neap tides on a macrotidal exposed coast. A calibrated and validated coupled hydrodynamic and wave numerical model of the South West UK was used.

5.1. Comparison With Observed Bedforms, Grain Size Distributions, and Literature

This study considers potential sand transport using a homogeneous medium sand bed. Further research integrating different sediment classes taken from observed size distributions could enable an assessment of the relative influence of tidal currents and waves on sediment transport paths for different sediment classes and the creation of an accurate regionalization for this area and a regional sediment budget based on realistic sediment availability. Much of the bed in this region is sand/gravelly sand, although areas of gravel, rock, and mud are present (Figure 5). Areas of gravel or rock correspond to strong potential sand transports predicted in the tide-only scenario, while areas of mud correspond to areas with very weak or negligible potential tidal sand transport.

In the Bristol Channel, a bed load parting zone is predicted (Figures 6 and 7), in agreement with previously published literature (Pingree & Griffiths, 1979), and supporting the bed load parting model argued by Stride and Belderson (1991). The region of the predicted divergences in the Bristol Channel coincides with rock and coarse sediment classes observed (Figure 5d) and erosional zones reported by McLaren et al. (1993), lending further support to the prediction. The Bristol Channel bed load parting zone is variable with the tidal state. During springs, the position of the bed load parting in sand transport extends between Porlock and Barry for all wave conditions. During neaps, the bed load parting moves up-channel reflecting the shift in the divergence of max bed shear stress (Figure 7). The presence of gravel barriers, such as observed at Porlock (Jennings et al., 1998; Orford & Jennings, 1998), matches the observation of Anthony (2002) that bed load parting of sand exposes gravel banks enhancing shoreward gravel reworking by storm waves and contributing to the formation of gravel barriers. These observations complement the observed sandwave morphology (Figures 5a–5c), further supporting the predictions of this model. Further work at this scale could examine hydrodynamic and wave controls on regional sandwave morphology and behavior (e.g., Campmans et al., 2018,Campmans et al., 2018; Damen et al., 2018).

Seaward residual currents occur in the deeper main channel of the Bristol Channel, matching lower resolution model results from Uncles (1982), partly driven by localized lowering of mean sea level at the seaward boundary relative to the Severn mouth. Return flow occurs in areas of low or negative gradients in tidal energy, such as embayments. A progressive tidal wave drives a progressively weakening northeast residual along the North Coast toward the Bristol Channel, matching modeled residuals published elsewhere at much lower resolution (Holt et al., 2001; Pingree & Le Cann, 1989). This drives a progressively weakening

northeast net sand transport, interrupted close to shore by several embayments, reaching insignificant levels near Bude Bay indicating that sand transport in this area is wave dominated, in agreement with coastal management reports (Motyka & Brampton, 1993; Welshby & Motyka, 1989). Residual circulation is enhanced in regions of strong topographic curvature such as headlands, around Land's End and islands such as Lundy and the Isles of Scilly. Consequently, these areas exhibit stronger tidal influence on potential sand transport.

Headlands are associated with tidal residual eddies with convergent sand transport, some matching the locations of well-known sand banks, such as Skerries Bank near Start Point (Pingree & Maddock, 1979). Convergence at these locations is enhanced during extreme waves. Headlands act as a focal point for tidal and wave energy, resulting in enhanced bed shear stresses and resuspension of sediments in these regions of higher residual currents and consequently the greatest potential sand transport rates (although in reality this will be limited by sediment availability; Carter et al., 1990; Draper et al., 2013; Uncles, 1982, 2010). Median waves enhance sand transport off headland tips in the tidal transport direction, whereas extreme waves can dominate sand transport direction, potentially causing a full reversal. This indicates that open coast, macrotidal, exposed, headland-bound embayments such as those along the North Coast are likely headland bypassing candidates, and the directionality of this process likely depends upon the incident wave height and direction (Goodwin et al., 2013; Klein et al., 2010; McCarroll et al., 2018; Vieira da Silva et al., 2016). Valiente et al. (2019) observed significant sediment transport beyond the depth of many headland cross-shore extents, challenging the notion of embayments being closed sediment cells. Higher-resolution modeling is required to examine the contribution of headland and embayment morphologic controls on headland sand bypassing during different conditions on a wider range of headland-bound embayments.

5.2. Wave-Induced Changes in Sand Transport Direction

Changes in net sand transport direction are evident between extreme wave, median wave, and tide-only conditions. These changes are presented in Figure 10, comparing both wave conditions with the tide-only prediction by subtracting the wave + tide from the tide-only transport directions. Little change in direction is observed at neap tide for median waves. Hydrodynamic and wave parameters and sand transport time series for example points I–VI are shown in Figures S3–S8 in the supporting information. Large direction changes are present offshore in the Approaches during springs, associated with variations in the weak tide-only transport direction (subplot I; Figure S3). A reversal in transport direction is predicted for outer Carmarthen Bay (subplot II; Figure S4) during median versus extreme waves, with net sand transport directed out of the embayment for median waves. Tide-only sand transport is weak here. Ebb asymmetry in current magnitude (strongest on the ebb) results in ebb asymmetry in bed shear stress and ebb-dominant sand transport for median waves. During extreme forcing, bed shear stress is modulated by water level, with a sustained increase over low water and a peak for waves propagating with the current (flood). Combined with a longer flood duration, this results in flood-dominated net sand transport for extreme waves.

At St. Ives Bay, sand transport around the west headland reverses from sand leaving to entering the bay (subplot IV; Figure S6). Tide-only and median wave depth-averaged velocity is ebb-asymmetric, with equal flood and ebb durations, driving ebb-dominated sand transport. Under extreme waves the currents become flood-asymmetric with a longer flood duration, driving flood-dominated sand transport. Changes in sand transport direction around headlands could have significant implications for adjacent beach response to extreme storms. Beaches on the west of St. Ives Bay accreted during the extreme 2013/2014 winter storms when other North Coast beaches experienced net erosion (Burvingt et al., 2017). The west side of St. Ives Bay is an area of convergence during extreme waves and divergence during tides only. Offshore from the North Coast sand transport vectors shift clockwise toward the shore under extreme waves, contrasting the median wave case (subplot III; Figure S5). Extreme wave spring sand transport vectors match closely those for neaps, where tide-only sand transport is effectively switched off, indicating that this shift results from wave dominance of sand transport.

The South Coast experiences a sand transport reversal south of Start Point under extreme waves, as the region of flood-dominated sand transport becomes ebb-dominant (subplot V; Figure S7). Tidal currents have flood asymmetry driving flood-dominated tidal and median wave sand transport. Tidal currents and elevations are in phase at this location, resulting in enhanced bed shear stress at low water (peak ebb) under wave forcing. The effect is greatest for extreme waves, driving a shift to ebb-dominant sand
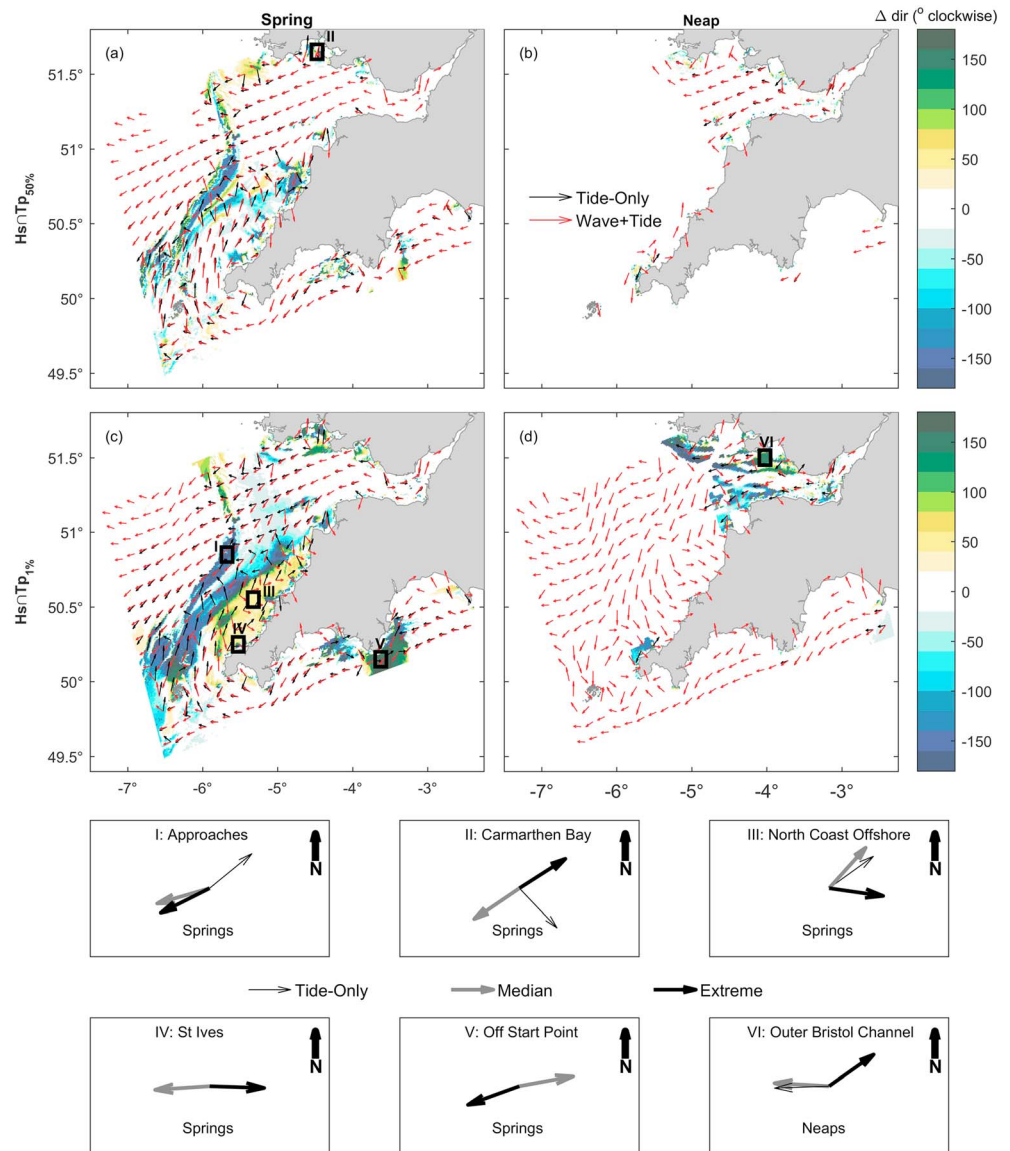
Figure 10. Changes in sand transport direction relative to the tide-only simulation for WNW wave forcing. Vectors represent net sand transport direction only. Red (black) arrows represent wave + tide (tide-only) forced sand transport direction. Areas of interest are marked and their sand transport directions shown in subplots I–VI. Bold arrows in I–VI represent wave forced transport with grey indicating median, black indicating extreme waves + tides; thin black arrows are tide-only.

transport. Porter-Smith et al. (2004) found that swell waves were most effective at mobilizing sediments at low water, and water-level variation must be considered when estimating sand transport in combined wave and tidal flows.

Extreme waves cause sand transport reversals in the margins of the outer Bristol Channel at neaps (subplot VI; Figure S8). Pattiaratchi and Collins (1988) reported this reversal for similar conditions observed at a point south of the Gower peninsula, shown here to be part of a broader directional trend of wave-dominated, up-channel directed transport during high-energy conditions at neaps. Currents at this location are ebb-asymmetric resulting in ebb asymmetry of bed shear stress for tides and median waves driving ebb-dominant sand transport. Under extreme waves, bed shear stress is modulated by water level with a sustained increase over low water. Enhanced wave impact at low water shifts net sand transport direction in the up-channel direction of wave propagation for low ebb velocities, resulting in a shorter period of ebb

than flood transport. Additionally, the sand transport magnitude is higher with waves following the current (flood) than opposing (ebb).

5.3. Classification of Wave/Tide Dominance

Net sand transport per tidal cycle for the tide-only, wave-only, and wave + tide simulations was used to determine the contribution from nonlinear wave-tide interactions, *NL*:

$$NL = WT - W - T \qquad (28)$$

where *WT*, *W*, and *T* are the combined wave + tide, wave-only, and tide-only net sand transports, respectively. Two ratios were used to determine first the relative influence of waves (including nonlinear wave-tide interactions) versus tides, and second the relative contribution of nonlinear wave-tide interactions versus waves alone. These ratios are

$$R1 = T : (W + NL), \qquad (29)$$

$$R2 = W : NL \qquad (30)$$

Increasing (decreasing) values of *R*1 indicate increasing tide (wave) dominance of sand transport. Regions with $R1 > 3$ were classified as "tide dominated," *T*. Further subdivision of regions where $R1 < 3$ was made using *R*2. Increasing values of *R*2 indicate increasing dominance of the wave-only contribution to net sand transport, while decreasing values indicate increasing nonlinear interaction dominance. Regions where $R1 < 1/3$ and $R2 > 3$ were classified as "wave dominated," *W*. Regions where $R1$ & $R2 < 1/3$ were classified as "nonlinear dominated," *NL*. The full classification is shown in Figure 11. Subdivisions are shown for intermediate ratios in the form "*A(b)*," where *A* indicates the dominant forcing and *(b)* indicates the subdominant forcing. For example, *W(t)* indicates wave-dominant sand transport with a subdominant tidal contribution. Regions where $1/3 < R1$ & $R2 < 3$ were classified as "mixed." From here on, wave dominance refers to "wave-dominated" regions, indicating wave-only sand transport is the major contribution to net sand transport per tidal cycle.

For median waves (Figures 11a and 11b), tides are dominant across much of the region except where tide-only sand transport is low and nonlinear wave-tide interactions become either a subdominant or dominant forcing. Median wave dominance at springs is isolated to shallow waters in North Coast embayments where tide-only sand transport is very low. Median wave dominance at neaps becomes more extensive along the North Coast, Isles of Scilly, and Carmarthen Bay where tide-only sand transport is negligible. At neaps, tide dominance is restricted mainly to the Upper Bristol Channel and off major promontories. Nonlinear interactions become dominant or subdominant in the Outer Bristol Channel where tide-only sand transport is weaker.

Tides are dominant up-channel of the upper Bristol Channel at springs, and up-channel of the Lower Severn at neaps for all wave conditions, due to wave attenuation and tidal flow constriction as it progresses up-channel resulting in larger tidal currents. These are the only regions that remain tide dominated under all conditions. Under extreme waves at springs (neaps), the Outer Bristol Channel becomes nonlinear (wave) dominated. The spatial pattern of transition to wave dominance under extreme waves at neaps in the Outer Bristol Channel (Figures 11b and 11d) matches the pattern of sand transport reversals seen in Figure 10d and observed by Pattiaratchi and Collins (1988), supporting the assertion of wave dominance in this area under these conditions.

The exposed North Coast becomes wave dominated under extreme waves (Figures 11c and 11d). Other areas of wave dominance are large embayments (e.g., Carmarthen Bay) and exposed areas of the South Coast. Propagation of WNW waves to the west facing stretches of the South Coast is evident in the pattern of wave/nonlinear dominance at neaps (Figure 11d). At neaps, extreme waves are dominant across much of the region, with a subdominant nonlinear interaction contribution. This is in agreement with predictions that waves cause significant additional net sand transport by enhancing transport in shallower, exposed regions where the tide-only contribution is small (van der Molen, 2002).
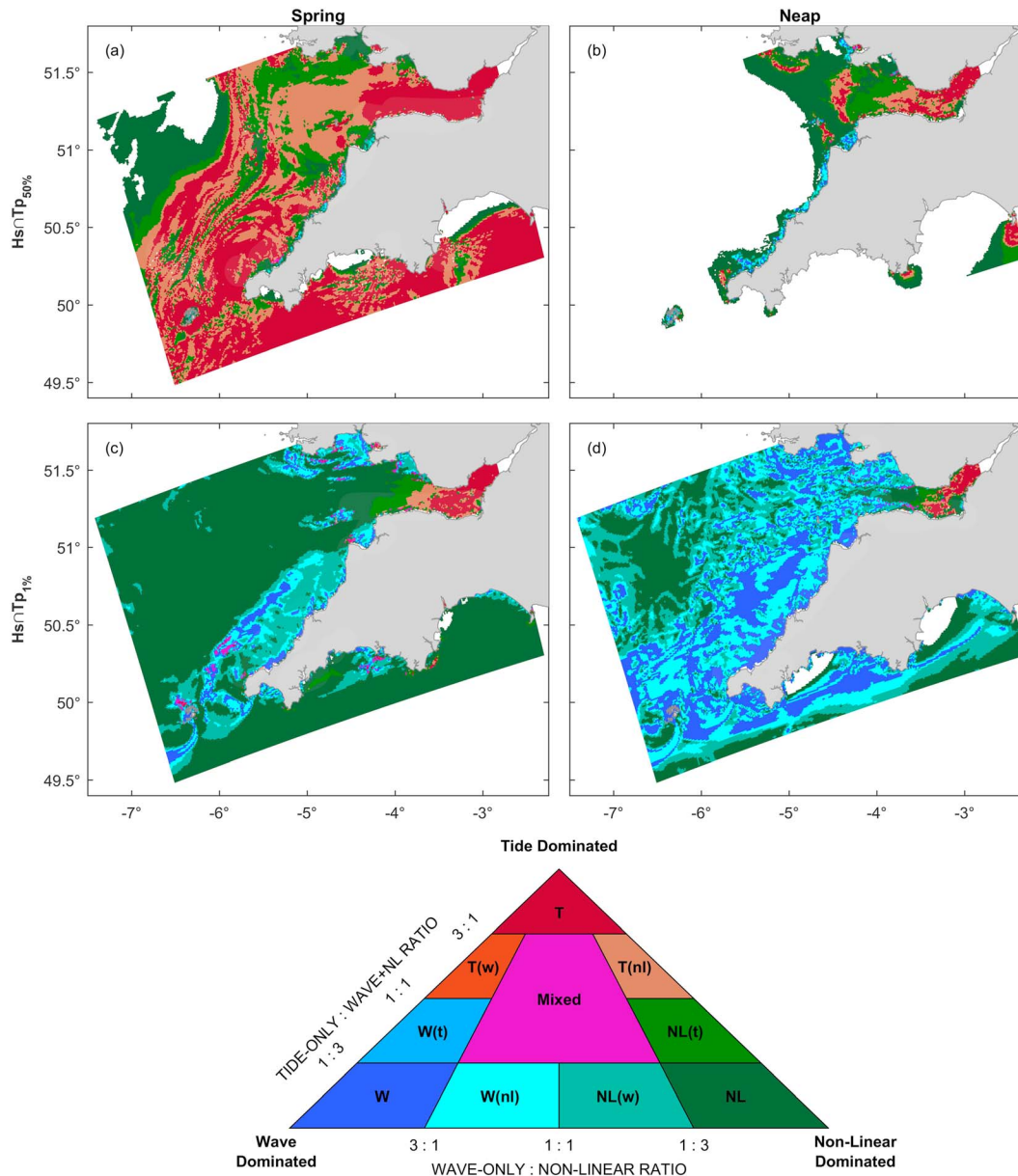
Figure 11. Wave-tide dominance classification of the South West UK during different wave and tide forcing, accounting for the relative influence of nonlinear wave-tide interactions. Based on potential net sand transport magnitude per tidal cycle, areas where wave + tide sand transport was <0.00016 m^3·m·cycle have been removed based on the transport formulation validation in van Rijn (2007b).

Nonlinear wave-tide interactions become the dominant forcing mechanism for sand transport across most of this macrotidal environment during 1% exceedance waves at springs (Figure 11c), contrasting wave dominance at neaps (Figure 11d). At neaps, nonlinear interactions significantly contribute to net sand transport, as shown in Figures 8, 11b, and 11d. This emphasizes the need for a fully coupled wave and hydrodynamic model for studies of sand transport paths in macrotidal and mesotidal environments exposed to extreme incident waves. The nonlinear effect of the interaction between waves and tides can significantly enhance sand transport beyond transport calculated for waves and tides in isolation.

This model considers depth-averaged hydrodynamics. Accordingly, some three-dimensional effects are parameterized, such as secondary flow generation by rotating current fields, or turbulence generation by breaking waves and enhanced bottom friction. Other processes are modeled in a depth-integrated

manner, such as the energy dissipation due to wave-breaking, whitecapping, and bottom friction. To investigate the potential impact of this on the results and classification scheme presented, a number of nonvalidated 3-D tests were conducted for the same scenarios using 10 terrain-following sigma layers and a $k - \epsilon$ turbulence scheme.

The impact of the addition of sigma layers was mainly to enhance the tide-only and wave-only net transport magnitude, with a larger relative increase in potential wave-related sand transport offshore in waters deeper than 60 m where net transport magnitudes are small. Offshore, low net transport regions shifted from purely nonlinear dominated NL to nonlinear dominated with a wave contribution NL(w) for extreme waves at springs, with wider spread wave dominance along the North Coast. There was more wave dominance for extreme waves at neaps, although the tide-dominated region in the upper Bristol Channel remained unchanged. Qualitatively, the spatial pattern of net sand transport remained the same, and the direction changes presented in Figure 10 were predominantly unchanged except for where weak tide-only sand transport was enhanced in the 3-D simulation. Nonlinear interactions remained dominant or subdominant across most of the domain during extreme wave forcing, supporting the conclusions presented here.

This classification has potential to be applied in other shelf areas; however, this currently requires a coupled hydrodynamic, wave, and sediment transport model. Further work could seek a predictive relationship for this classification based on readily available tide and wave data. Many regions globally experience high wave and tidal energy. Harris and Coleman (1998) estimate that swell waves were able to mobilize 0.1-mm quartz sand over 41.6% of the Earth's continental shelves over three years. Waves dominate sediment transport in areas of the New Zealand and Australian shelves (Carther & Heath, 1975; Hale et al., 2014; Moriarti et al., 2014; Porter-Smith et al., 2004). Wave-current interactions are significant drivers of sediment resuspension on the Northwest Iberian shelf (Zhang et al., 2016). The Northwest European shelf experiences high tidal and high wave energy, which is enhanced by wave-current interactions in areas of strong tidal currents (Hashemi & Neill, 2014). Sand transport on the UK east coast was designated as tide dominated by van der Molen (2002), ignoring wave-current interactions. However, the results of this study suggest that wave-tide interactions can have a significant impact on net sand transport even for median waves. This classification scheme should be tested in similar environments globally to test for wave, tide, or nonlinear interaction dominance of sediment transport.

6. Conclusions

1. A Delft3D numerical model was used to investigate the relative influence of tidal and wave forcing on potential sand transport in an energetic, exposed, macrotidal environment. The South West UK was used as a test site with a uniform medium sand bed allowing direct comparison between different regions. Waves were forced with median (50% exceedance) and extreme (1% exceedance) wave scenarios from two modal directions at spring and neap tides. Tide-only, wave-only, and fully coupled scenarios were simulated for all forcing combinations.
2. Bed load transport directions match observed sandwave asymmetry and orientations for tides-only and previously published observations under energetic waves. Regions of the greatest potential sand transport or major divergence correspond to observed coarse sediment classes. These observations indicate a potential sand transport approach can give indications of sediment transport pathways, divergences, and likely size distributions in the absence of detailed observations.
3. Sand transport across this macrotidal environment is heavily influenced by waves. The greatest influence is in areas fully exposed to the incident wave forcing. Extreme waves increase potential sand transport by over an order of magnitude, and are capable of mobilizing medium sand below 120-m depth.
4. Waves can strongly influence sand transport direction. Median waves predominantly enhance sand transport in the tidal direction, whereas extreme waves are able to induce directional shifts and full reversals.
5. Tidal forcing is more important around headlands and islands, and in regions where constriction of the tidal wave produces strong tidal currents. Elsewhere, tidal forcing is significant only at springs, and is effectively switched off during neaps except under extreme waves.
6. A new classification scheme was created for the region in terms of tide-only, wave-only, or nonlinear wave-tide interaction dominance of net sand transport with potential for application elsewhere.

7. During median waves at springs the whole region is tide dominated apart from where tidal sand transport is weakest. Wave dominance is restricted to shallow embayments fully exposed to the incident waves.

8. Wave-tide interactions (encompassing radiation stresses, stokes drift, enhanced bottom friction, enhanced bed shear stress, current and depth-induced wave refraction, Doppler shift, and wave blocking) nonlinearly enhance net sand transport. These processes are dominant or subdominant across most of the region during extreme waves for all tide conditions, and during median waves at neaps, apart from where the tidal constriction and wave attenuation are greatest. This implies a critical need to consider the impact of wave-tide interactions on regional sand transport patterns on energetic, exposed continental shelves globally.

References

Anthony, E. J. (2002). Long-term marine bedload segregation, and sandy versus gravelly Holocene shorelines in the eastern English Channel. *Marine Geology*, *187*(3-4), 221–234. https://doi.org/10.1016/S0025-3227(02)00381-X

Bentamy, A., & Fillon, D. C. (2012). Gridded surface wind fields from Metop/ASCAT measurements. *International Journal of Remote Sensing*, *33*(6), 1729–1754. https://doi.org/10.1080/01431161.2011.600348

Booij, N., Holthuijsen, L. H., & Ris, R. C. (1999). A third-generation wave model for coastal regions 1. Model description and validation. *Journal of Geophysical Research*, *104*(C4), 7649–7666. https://doi.org/10.1029/98JC02622

Bricheno, L. M., Wolf, J., & Aldridge, J. (2015). Distribution of natural disturbance due to wave and tidal bed currents around the UK. *Continental Shelf Research*, *109*, 67–77. https://doi.org/10.1016/j.csr.2015.09.013

Brown, J. M., Bolaños, R., Howarth, M. J., & Souza, A. J. (2012). Extracting sea level residual in tidally dominated estuarine environments. *Ocean Dynamics*, *62*(7), 969–982. https://doi.org/10.1007/s10236-012-0543-7

Burvingt, O., Masselink, G., Russell, P., & Scott, T. (2017). Classification of beach response to extreme storms. *Geomorphology*, *295*, 722–737. https://doi.org/10.1016/j.geomorph.2017.07.022

Campmans, G. H. P., Roos, P. C., de Vriend, H. J., & Hulscher, S. J. M. H. (2018). The influence of storms on sandwave evolution: A nonlinear idealized modeling approach. *Journal of Geophysical Research: Earth Surface*, *123*, 2070–2086. https://doi.org/10.1029/2018JF004616

Campmans, G. H. P., Roos, P. C., Schrijen, E. P. W. J., & Hulscher, S. J. M. H. (2018). Modeling wave and wind climate effects on tidal sandwave dynamics: A North Sea case study. *Estuarine, Coastal and Shelf Science*, *213*, 137–147. https://doi.org/10.1016/j.ecss.2018.08.015

Carruthers, J. N. (1963). History, sandwaves and near-bed currents of La Chapelle Bank. *Nature*, *197*(4871), 942–946. https://doi.org/10.1038/197942a0

Carter, R. W. G., Jennings, S. C., & Orford, J. D. (1990). Headland erosion by waves. *Journal of Coastal Research*, *6*(3), 517–529. http://www.jstor.org/stable/4297714

Carther, L., & Heath, R. A. (1975). Role of mean circulation, tides and waves in the transport of bottom sediment on the New Zealand continental shelf. *New Zealand Journal of Marine and Freshwater Research*, *9*(4), 423–448. https://doi.org/10.1080/00288330.1975.9515579

Castelle, B., Dodet, G., Masselink, G., & Scott, T. (2017). A new climate index controlling winter wave activity along the Atlantic coast of Europe: The West Europe Pressure Anomaly. *Geophysical Research Letters*, *44*, 1384–1392. https://doi.org/10.1002/2016GL072379

Castelle, B., Dodet, G., Masselink, G., & Scott, T. (2018). Increased winter-mean wave height, variability and periodicity in the North-East Atlantic over 1949–2017. *Geophysical Research Letters*, *45*, 3586–3596. https://doi.org/10.1002/2017GL076884

Channon, R. D., & Hamilton, D. (1976). Wave and tidal current sorting of shelf sediments southwest of England. *Sedimentology*, *23*(1), 17–42. https://doi.org/10.1111/j.1365-3091.1976.tb00037.x

Codiga, D. L. (2011). Unified tidal analysis and prediction using the UTide Matlab functions. URI/GSO Technical Report 2011-01, pp. 1–59. Graduate School of Oceanography, University of Rhode Island, Narragansett, RI. https://doi.org/10.13140/RG.2.1.3761.2008

Collins, M. B. (1987). Sediment transport in the Bristol Channel: A review. *Proceedings of the Geologists' Association*, *98*(4), 367–383. https://doi.org/10.1016/S0016-7878(87)80076-7

Collins, M. B., Ferentinos, G., & Banner, F. T. (1979). The hydrodynamics and sedimentology of a high (tidal and wave) energy embayment (Swansea Bay, northern Bristol Channel). *Estuarine and Coastal Marine Science*, *8*(1), 49–74. https://doi.org/10.1016/0302-3524(79)90105-1

Damen, J. M., van Dijk, T. A. G. P., & Hulscher, S. J. M. H. (2018). Spatially Varying Environmental Properties Controlling Observed Sand Wave Morphology. *Journal of Geophysical Research: Earth Surface*, *123*(2), 262–280. https://doi.org.10.1002/2017jf004322

Deltares. (2014). Delft3D-FLOW, Simulation of multi-dimensional hydrodynamic flows and transport phenomena, including sediments. User Manual: Hydro-Morphodynamics. Version 3.15.34158. Delft, The Netherlands: Deltares.

Dietrich, J. C., Zijlema, M., Westerink, J. J., Holthuijsen, L. H., Dawson, C., Luettich, R. A. Jr., et al. (2011). Modeling hurricane waves and storm surge using integrally-coupled, scalable computations. *Coastal Engineering*, *58*(1), 45–65. https://doi.org/10.1016/j.coastaleng.2010.08.001

Dingemans, M. W., Radder, A. C., & De Vriend, H. J. (1987). Computation of the driving forces of wave-induced currents. *Coastal Engineering*, *11*(5-6), 539–563. https://doi.org/10.1016/0378-3839(87)90026-3

Donal, M. G., Renggli, D., Wild, S., Alexander, L. V., Leckebusch, G. C., & Ulbrich, U. (2011). Reanalysis suggests long-term upward trends in European storminess since 1871. *Geophysical Research Letters*, *38*, L14703. https://doi.org/10.1029/2011GL047995

Draper, L. (1967). Wave activity at the sea bed around northwestern Europe. *Marine Geology*, *5*(2), 133–140. https://doi.org/10.1016/0025-3227(67)90075-8

Draper, S., Borthwick, A. G. L., & Houlsby, G. T. (2013). Energy potential of a tidal fence deployed near a coastal headland. *Philosophical Transactions of the Royal Society A*, *371*(1985). https://doi.org/10.1098/rsta.2012.0176

Elias, E. P. L., Gelfenbaum, G., & Van der Westhuysen, A. J. (2012). Validation of a coupled wave-flow model in a high-energy setting: The mouth of the Columbia River. *Journal of Geophysical Research*, *117*, C09011. https://doi.org/10.1029/2012JC008105

EMODnet Bathymetry Consortium. (2016). EMODnet Digital Bathymetry (DTM 2016). EMODnet Bathymetry Consortium. https://doi.org/10.12770/c7b53704-999d-4721-b1a3-04ec60c87238

Folk, R. L. (1954). The distinction between grain size and mineral composition in sedimentary rock nomenclature. *Journal of Geology*, *62*(4), 344–359. www.jstor.org/stable/30065016, https://doi.org/10.1086/626171

Fong, S. W., & Heaps, N. S. (1978). *Note on quarter-wave tidal resonance in the Bristol Channel. (Institute of Oceanographic Sciences Report No. 6)*, *UK. Institute of Oceanographic Sciences*, (p. 11). https://eprints.soton.ac.uk/id/eprint/14346

Fredsøe, J. (1984). Turbulent boundary layer in wave-current motion. *Journal of Hydraulic Engineering*, *110*(8), 1103–1120. https://doi.org/10.1061/(ASCE)0733-9429(1984)110:8(1103

Genest, C., & Favre, A.-C. (2007). Everything you always wanted to know about copula modeling but were afraid to ask. Journal of Hydrologic Engineering. *12*(4), 347–368. https://doi.org/10.1061/(ASCE)1084-0699(2007)12:4(347)

Goodwin, I. D., Freeman, R., & Blackmore, K. (2013). An insight into headland sand bypassing and wave climate variability from shoreface bathymetric change at Byron Bay, New South Wales, Australia. *Marine Geology*, *341*, 29–45. https://doi.org/10.1016/j.margeo.2013.05.005

Graham, J. A., O'Dea, E., Holt, J., Polton, J., Hewitt, H. T., Furner, R., et al. (2018). AMM15: a new high-resolution NEMO configuration for operational simulation of the European north-west shelf. *Geoscientific Model Development*, *11*(2), 681–696. https://doi.org/10.5194/gmd-11-681-2018

Grant, W. D., & Madsen, O. S. (1979). Combined wave and current interaction with a rough bottom. *Journal of Geophysical Research*, *84*(C4), 1797–1808. https://doi.org/10.1029/JC084iC04p01797

Grant, W. D., & Madsen, O. S. (1986). The continental-shelf bottom boundary layer. *Annual Review of Fluid Mechanics*, *18*(1), 265–305. https://doi.org/10.1146/annurev.fl.18.010186.001405

Grunnet, N. M., Walstra, D. J. R., & Ruessink, B. G. (2004). Process-based modelling of a shoreface nourishment. *Coastal Engineering*, *51*(7), 581–607. https://doi.org/10.1016/j.coastaleng.2004.07.016

Hadley, M. L. (1964). Wave-induced bottom currents in the Celtic Sea. *Marine Geology*, *2*(1–2), 164–167. https://doi.org.10.1016/0025-3227(64)90033-7

Hale, R. P., Ogston, A. S., Walsh, J. P., & Orpin, A. R. (2014). Sediment transport and event deposition on the Waipaoa River Shelf, New Zealand. *Continental Shelf Research*, *86*, 52–65. https://doi.org/10.1016/j.csr.2014.01.009

Hanley, J., & Caballero, R. (2012). The role of large-scale atmospheric flow and Rossby wave breaking in the evolution of extreme wind-storms over Europe. *Geophysical Research Letters*, *39*, L21708. https://doi.org/10.1029/2012GL053408

Hansen, J. E., Elias, E., List, J. H., Erikson, L. H., & Barnard, P. L. (2013). Tidally influenced alongshore circulation at an inlet-adjacent shoreline. *Continental Shelf Research*, *56*, 26–38. https://doi.org/10.1016/j.csr.2013.01.017

Harris, P. T., & Coleman, R. (1998). Estimating global shelf sediment mobility due to swell waves. *Marine Geology*, *150*(1-4), 171–177. https://doi.org/10.1016/S0025-3227(98)00040-1

Harris, P. T., & Collins, M. B. (1991). Sand transport in the Bristol Channel: Bedload parting zone or mutually evasive transport pathways? *Marine Geology*, *101*(1-4), 209–216. https://doi.org/10.1016/0025-3227(91)90072-C

Hashemi, M. R., & Neill, S. P. (2014). The role of tides in shelf-scale simulations of the wave energy resource. *Renewable Energy*, *69*, 300–310. https://doi.org/10.1016/j.renene.2014.03.052

Hashemi, M. R., Neill, S. P., & Davies, A. G. (2014). A coupled tide-wave model for the NW European shelf seas. *Geophysical & Astrophysical Fluid Dynamics*, *109*(3), 234–253. https://doi.org/10.1080/03091929.2014.944909

Heathershaw, A. D., New, A. L., & Edwards, P. D. (1987). Internal tides and sediment transport at the shelf break in the Celtic Sea. *Continental Shelf Research*, *7*(5), 485–517. https://doi.org/10.1016/0278-4343(87)90092-6

Herrling, G., & Winter, C. (2018). Tidal inlet sediment bypassing at mixed-energy barrier islands. *Coastal Engineering*, *140*, 342–354. https://doi.org/10.1016/j.coastaleng.2018.08.008

Holt, J., Hyder, P., Ashworth, M., Harle, J., Hewitt, H. T., Liu, H., et al. (2017). Prospects for improving the representation of coastal and shelf seas in global ocean models. *Geoscientific Model Development*, *10*(1), 499–523. https://doi.org/10.5194/gmd-10-499-2017

Holt, J. T., James, I. D., & Jones, E. J. (2001). An s coordinate density evolving model of the northwest European continental shelf: 2. Seasonal currents and tides. *Journal of Geophysical Research*, *106*(C7), 14,035–14,053. https://doi.org/10.1029/2000JC000303

Holt, J. T., & Proctor, R. (2008). The seasonal circulation and volume transport on the northwest European continental shelf: A fine-resolution model study. *Journal of Geophysical Research*, *113*, C06021. https://doi.org/10.1029/2006JC004034

Hopkins, J., Elgar, S., & Raubenheimer, B. (2015). Observations and model simulations of wave-current interaction on the inner shelf. *Journal of Geophysical Research: Oceans*, *121*, 198–208. https://doi.org/10.1002/2015JC010788

Jennings, S., Orford, J. D., Canti, M., Devoy, R. J. N., & Straker, V. (1998). The role of relative sea-level rise and changing sediment supply on Holocene gravel barrier development: The example of Porlock, Somerset, UK. *The Holocene*, *8*(2), 165–181. https://doi.org/10.1191/095968398667901806

Kalkwijk, J. P. T., & Booij, R. (1986). Adaptation of secondary flow in nearly horizontal flow. *Journal of Hydraulic Research*, *24*(1), 19–37. https://doi.org/10.1080/00221688609499330

Kemp, P. H., & Simmons, R. R. (1982). The interaction between waves and a turbulent current: Waves propagating with the current. *Journal of Fluid Mechanics*, *116*, 227–250. https://doi.org/10.1017/S0022112082000445

Kemp, P. H., & Simmons, R. R. (1983). The interaction of waves and a turbulent current: Waves propagating against the current. *Journal of Fluid Mechanics*, *130*(1), 73–89. https://doi.org/10.1017/S0022112083000981

Klein, A. H. F., Ferreira, Ó., Dias, J. M. A., Tessler, M. G., Silveira, L. F., Benedet, L., et al. (2010). Morphodynamics of structurally con-trolled headland-bay beaches in southeastern Brazil: A review. *Coastal Engineering*, *57*(2), 98–111. https://doi.org/10.1016/j.coastaleng.2009.09.006

Klopman, G. (1994). Vertical structure of the flow due to waves and currents. Progress report H840.30, Part II. Delft Hydraulics.

Knaapen, M. A. F. (2005). Sandwave migration predictor based on shape information. *Journal of Geophysical Research*, *110*, F04S11. https://doi.org/10.1029/2004JF000195

Leonardi, N., Kolker, A. S., & Fagherazzi, S. (2015). Interplay between river discharge and tides in a delta distributary. *Advances in Water Resources*, *80*, 69–78. https://doi.org/10.1016/j.advwatres.2015.03.005

Leonardi, N., & Plater, A. J. (2017). Residual flow patterns and morphological changes along a macro- and meso-tidal coastline. *Advances in Water Resources*, *109*, 290–301. https://doi.org/10.1016/j.advwatres.2017.09.013

Lesser, G. R., Roelvink, J. A., Van Kester, J. A. T. M., & Stelling, G. S. (2004). Development and validation of a three-dimensional morphological model. *Coastal Engineering*, *51*(8-9), 883–915. https://doi.org/10.1016/j.coastaleng.2004.07.014

Lewis, M. J., Neill, S. P., & Elliot, A. J. (2015). Interannual variability of two offshore sand banks in a region of extreme tidal range. *Journal of Coastal Research*, *300*(2), 265–275. https://doi.org/10.2112/JCOASTRES-D-14-00010.1

Lin, B., & Falconer, R. A. (2001). Numerical modelling of 3-D tidal currents and water quality indicators in the Bristol Channel. *Proceedings of the Institution of Civil Engineers - Water and Maritime Engineering*, *148*(3), 155–166. https://doi.org/10.1680/wame.2001.148.3.155

Lopez, G., Conley, D. C., & Greaves, D. (2016). Calibration, validation, and analysis of an empirical algorithm for the retrieval of wave spectra from HF radar sea echo. *Journal of Atmospheric and Oceanic Technology*, *33*(2), 245–261. https://doi.org/10.1175/JTECH-D-15-0159.1

Luijendijk, A. P., Ranasinghe, R., de Schipper, M. A., Huisman, B. A., Swinkels, C. M., Walstra, D. J. R., & Stive, M. J. F. (2017). The initial morphological response of the Sand Engine: A process-based modelling study. *Coastal Engineering*, *119*, 1–14. https://doi.org/10.1016/j.coastaleng.2016.09.005

Lyddon, C., Brown, J. M., Leonardi, N., & Plater, A. J. (2018). Flood hazard assessment for a hyper-tidal estuary as a function of tide-surge-morphology interaction. *Estuaries and Coasts*, *41*(6), 1565–1586. https://doi.org/10.1007/s12237-018-0384-9

Marmorino, G. O., & Hallock, Z. R. (2001). On estimating wind velocity using an upward-looking ADCP. *Journal of Atmospheric and Oceanic Technology*, *8*(5), 791–798. https://doi.org/10.1175/1520-0426(2001)018<0791:OEWVUA>2.0.CO;2

Masselink, G., Castelle, B., Scott, T., Dodet, G., Suanez, S., Jackson, D., & Floc'h, F. (2016). Extreme wave activity during 2013/14 winter and morphological impacts along the Atlantic coast of Europe. *Geophysical Research Letters*, *43*, 2135–2143. https://doi.org/10.1002/2015GL067492

Masselink, G., Scott, T., Poate, T., Russell, P., Davidson, M., & Conley, D. (2015). The extreme 2013/14 winter-storms: Hydrodynamic forcing and coastal response along the southwest coast of England. *Earth Surface Processes and Landforms*, *41*(3), 378–391. https://doi.org/10.1002/esp.3836

McCarroll, R. J., Masselink, G., Valiente, N. G., Scott, T., King, E. V., & Conley, D. (2018). Wave and tidal controls on embayment circulation and headland bypassing for an exposed, macrotidal site. *Journal of Marine Science and Engineering*, *6*(3), 94. https://doi.org/10.3390/jmse6030094

McConnell, N., King, R., Tonani, M., O'Dea, E., Martin, M., Sykes, P. & Ryan, A. (2017). North West European Shelf Production Centre NORTHWESTSHELF_ANALYSIS_FORECAST_PHYS_004_001_b. Quality Information Document. Issue 3.5. Copernicus Marine Environment Monitoring Service.

McLaren, P., Collins, M. B., Gao, S., & Powys, R. I. L. (1993). Sediment dynamics of the Severn Estuary and inner Bristol Channel. *Journal of the Geological Society*, *150*(3), 589–603. https://doi.org/10.1144/gsjgs.150.3.0589

Mori, N., Sizuki, T., & Kakuno, S. (2007). Noise of acoustic Doppler velocimeter data in bubbly flows. *Journal of Engineering Mechanics*, *133*(1), 122–125. https://doi.org/10.1061/(ASCE)0733-9399(2007)133:1(122)

Moriarti, J. M., Harris, C. K., & Hadfield, M. G. (2014). A hydrodynamic and sediment transport model for the Waipaoa Shelf, New Zealand: sensitivity of fluxes to spatially-varying erodibility and model nesting. *Journal of Marine Schence and Engineering*, *2*(2), 336–369. https://doi.org/10.3390/jmse2020336

Motyka, J. M. & Brampton, A. H. (1993). Coastal management. Mapping of littoral cells. HR Wallingford Ltd, Report SR 328. http://eprints.hrwallingford.co.uk/748/1/SR328.pdf

Murphy, A. H., & Epstein, E. S. (1989). Skill scores and correlation coefficients in model verification. *Monthly Weather Review*, *117*(3), 572–582. https://doi.org/10.1175/1520-0493(1989)117<0572:SSACCI>2.0.CO;2

Neill, S. P., Scourse, J. D., & Uehara, K. (2010). Evolution of bed shear stress distribution over the northwest European shelf seas during the last 12,000 years. *Ocean Dynamics*, *60*(5), 1139–1156. https://doi.org/10.1007/s10236-010-0313-3

Nielsen, P. (1992). *Coastal bottom boundary layers and sediment transport*. Singapore: World Scientific Publishing Co. Pte. Ltd. https://doi.org/10.1142/1269

O'Dea, E. J., Arnold, A. K., Edwards, K. P., Furner, R., Hyder, P., Martin, M. J., et al. (2012). An operational ocean forecast system incorporating NEMO and SST data assimilation for the tidally driven European North-West shelf. *Journal of Operational Oceanography*, *5*(1), 3–17. https://doi.org/10.1080/1755876X.2012.11020128

Olabarrieta, M., Medina, R., & Castenedo, S. (2010). Effects of wave–current interaction on the current profile. *Coastal Engineering*, *57*(7), 643–655. https://doi.org/10.1016/j.coastaleng.2010.02.003

Orford, J., & Jennings, S. (1998). 8: The importance of different time-scale controls on coastal management strategy: The problem of Porlock gravel barrier, Somerset, UK. In J. M. Hooke (Ed.), *Coastal defence and earth science conservation*, (pp. 87–102). Bath, UK: The Geological Society.

Pattiaratchi, C., & Collins, M. C. (1988). Wave influence on coastal sand transport paths in a tidally dominated environment. *Ocean & Shore Management*, *11*(6), 449–465. https://doi.org/10.1016/0951-8312(88)90025-2

Pingree, R. D., & Griffiths, D. K. (1979). Sand transport paths around the British Isles resulting from M_2 and M_4 tidal interactions. *Journal of the Marine Biological Association of the United Kingdom*, *59*(2), 497–513. https://doi.org/10.1017/S0025315400042806

Pingree, R. D., & Griffiths, D. K. (1980). Currents driven by a steady uniform wind stress on the shelf areas around the British Isles. *Oceanologica Acta*, *3*, 227–236. http://archimer.ifremer.fr/doc/00121/23265/

Pingree, R. D., & Le Cann, B. (1989). Celtic and Amorican slope and shelf residual currents. *Progress in Oceanography*, *23*(4), 303–338. https://doi.org/10.1016/0079-6611(89)90003-7

Pingree, R. D., & Maddock, L. (1977). Tidal eddies and coastal discharge. *Journal of the Marine Biological Association of the United Kingdom*, *57*(3), 869–875. https://doi.org/10.1017/S0025315400025224

Pingree, R. D., & Maddock, L. (1979). The tidal physics of headland flows and offshore tidal bank formation. *Marine Geology*, *32*(3-4), 269–289. https://doi.org/10.1016/0025-3227(79)90068-9

Porter-Smith, R., Harris, P. T., Andersen, O. B., Coleman, R., Greenslade, D., & Jenkins, C. J. (2004). Classification of the Australian continental shelf based on predicted sediment threshold exceedance from tidal currents and swell waves. *Marine Geology*, *211*(1-2), 1–20. https://doi.org/10.1016/j.margeo.2004.05.031

Prodger, S., Russell, P., & Davidson, M. (2017). Grain-size distributions on high-energy sandy beaches and their relation to wave dissipation. *Sedimentology*, *64*(5), 1289–1302. https://doi.org/10.1111/sed.12353

Reynaud, J.-Y., Tessier, B., Berné, S., Hervé, C., & Debatist, M. (1999). Tide and wave dynamics on a sand bank from the deep shelf of the Western Channel approaches. *Marine Geology*, *161*(2-4), 339–359. https://doi.org/10.1016/S0025-3227(99)00033-X

Ridderinkhof, W., Swart, H. E., Vegt, M., & Hoekstra, P. (2016). Modeling the growth and migration of sandy shoals on ebb-tidal deltas. *Journal of Geophysical Research: Earth Surface*, *121*, 1351–1372. https://doi.org/10.1002/2016JF003823

Saha, S., Moorthi, S., Wu, X., Wang, J., Nadiga, S., Tripp, P., et al. (2014). The NCEP Climate Forecast System version 2. *Journal of Climate*, *27*(6), 2185–2208. https://doi.org/10.1175/JCLI-D-12-00823.1

Saulter, A. (2017). North West European Shelf Production Centre: NORTHWESTSHELF_ANALYSIS_FORECAST_WAV_004_012. Quality Information Document. Issue 1.0. Copernicus Marine Environment Monitoring Service.

Scott, T., Masselink, G., O'Hare, T., Saulter, A., Poate, T., Russell, P., et al. (2016). The extreme 2013/2014 winter storms: Beach recovery along the southwest coast of England. *Marine Geology*, *382*, 224–241. https://doi.org/10.1016/j.margeo.2016.10.011

Soulsby, R. L., Hamm, L., Klopman, G., Myrhaug, D., Simons, R. R., & Thomas, G. P. (1993). Wave-current interaction within and outside the bottom boundary layer. *Coastal Engineering*, *21*(1-3), 41–69. https://doi.org/10.1016/0378-3839(93)90045-a

Stride, A. H. (1963). Current-swept sea floors near the southern half of Great Britain. *Quarterly Journal of the Geological Society*, *119*(1-4), 175–197. https://doi.org/10.1144/gsjgs.119.1.0175

Stride, A. H., & Belderson, R. H. (1990). A reassessment of sand transport paths in the Bristol Channel and their regional significance. *Marine Geology*, *92*(3-4), 227–236. https://doi.org/10.1016/0025-3227(90)90005-5

Stride, A. H., & Belderson, R. H. (1991). Sand transport in the Bristol Channel east of Bull Point and Worms Head: A bed-load parting model with some indications of mutually evasive sand transport paths. *Marine Geology*, *101*(1-4), 203–207. https://doi.org/10.1016/0025-3227(91)90071-B

Sutherland, J., Peet, A. H., & Soulsby, R. L. (2004). Evaluating the performance of morphological models. *Coastal Engineering*, *51*(8-9), 917–939. https://doi.org/10.1016/j.coastaleng.2004.07.015

Tambroni, N., Blondeaux, P., & Giovanna, V. (2015). A simple model of wave-current interaction. *Journal of Fluid Mechanics*, *775*, 328–348. https://doi.org/10.1017/jfm.2015.308

Taylor, G. I. (1921). Tides in the Bristol Channel. *Mathematical Proceedings of the Cambridge Philosophical Society*, *20*, 320–325.

Thompson, C. E. L., Williams, M. E., Amoudry, L., Hull, T., Reynolds, S., Panton, A., & Fones, G. R. (2017). Benthic controls of resuspension in UK shelf seas: Implications for resuspension frequency. *Continental Shelf Research*. https://doi.org/10.1016/j.csr.2017.12.005

Turner, J. F., Iliffe, J. C., Ziebart, M. K., Wilson, C., & Horsburgh, K. J. (2010). Interpolation of tidal levels in the coastal zone for the creation of a hydrographic datum. *Journal of Atmospheric and Ocean Technology*, *27*(3), 605–613. https://doi.org/10.1175/2009JTECHO645.1

Umeyama, M. (2005). Reynolds stresses and velocity distributions in a wave–current coexisting environment. *Journal of Waterway, Port, Coastal and Ocean Engineering*, *131*(5), 203–212. https://doi.org/10.1061/(ASCE)0733-950X(2005)131:5(203

Uncles, R. J. (1982). Computed and observed residual currents in the Bristol Channel. *Oceanologica Acta*, *5*(1), 11–20. http://archimer.ifremer.fr/doc/00120/23148/

Uncles, R. J. (1984). Hydrodynamics of the Bristol Channel. *Marine Pollution Bulletin*, *15*(2), 47–53. https://doi.org/10.1016/0025-326X(84)90461-2

Uncles, R. J. (2010). Physical properties and processes in the Bristol Channel and Severn Estuary. *Marine Pollution Bulletin*, *61*(1-3), 5–20. https://doi.org/10.1016/j.marpolbul.2009.12.010

Valiente, N. G., Masselink, G., Scott, T., Conley, D. C., & McCarroll, R. J. (2019). Role of waves and tides on depth of closure and potential for headland bypassing. *Marine Geology*, *407*, 60–75. https://doi.org/10.1016/j.margeo.2018.10.009

van der Molen, J. (2002). The influence of tides, wind and waves on the net sand transport in the North Sea. *Continental Shelf Research*, *22*(18-19), 2739–2762. https://doi.org/10.1016/S0278-4343(02)00124-3

van Rijn, L. C. (2007a). Unified view of sediment transport by currents and waves. I: Initiation of motion, bed roughness, and bed-load transport. *Journal of Hydraulic Engineering.*, *133*(6), 649–667. https://doi.org/10.1061/(ASCE)0733-9429(2007)133:6(649

van Rijn, L. C. (2007b). Unified view of sediment transport by currents and waves. II: Suspended transport. *Journal of Hydraulic Engineering*, *133*(6), 668–689. https://doi.org/10.1061/(ASCE)0733-9429(2007)133:6(668

van Rijn, L. C., Roelvink, J. A. & Horst, W. T. (2000). Approximation formulae for sand transport by currents and waves and implementation in DELFT-MOR. Technical Report Z3054.40. Delft, The Netherlands: WL Delft Hydraulics.

van Rijn, L. C., Walstra, D. J. R. & van Ormondt, M. (2004). Description of TRANSPOR2004 and implementation in Delft3D-ONLINE, Final Report. Report Z3748.10. Delft, The Netherlands: WL Delft Hydraulics.

Verschelling, E., Deijl, E., Perk, M., Sloff, K., & Middelkoop, H. (2017). Effects of discharge, wind, and tide on sedimentation in a recently restored tidal freshwater wetland. *Hydrological Processes*, *31*(16), 2827–2841. https://doi.org/10.1002/hyp.11217

Vieira da Silva, G., Toldo, E. E. Jr., da Klein, A. H. F., Short, A. D., & Woodroffe, C. D. (2016). Headland sand bypassing—Quantification of net sediment transport in embayed beaches, Santa Catarina Island North Shore, Southern Brazil. *Marine Geology*, *379*, 13–27. https://doi.org/10.1016/j.margeo.2016.05.008

Ward, S. L., Neill, S. P., Van Landeghem, K. J. J., & Scourse, J. D. (2015). Classifying seabed sediment type using simulated tidal-induced bed shear stress. *Marine Geology*, *367*, 94–104. https://doi.org/10.1016/j.margeo.2015.05.010

Welshby, J. & Motyka, J. M. (1989). A macro review of the coastline of England and Wales. Volume 6. The South West Coast. Portland Bill to Avonmouth. Hydraulics Research Limited, Report SR 192. http://eprints.hrwallingford.co.uk/1263/1/SR192.pdf

Willmott, C. J., & Matsuura, K. (2005). Advantages of the mean absolute error (MAE) over the root mean square error (RMSE) in assessing average model performance. *Climate Research*, *30*, 79–82. https://doi.org/10.3354/cr030079

Willmott, C. J., Robeson, S. M., & Matsuura, K. (2012). A refined index of model performance. *International Journal of Climatology*, *32*(13), 2088–2094. https://doi.org/10.1002/joc.2419

Xia, J., Falconer, R. A., & Lin, B. (2010). Numerical model assessment of tidal stream energy resources in the Severn Estuary, UK. *Proceedings of the Institution of Mechanical Engineers, Part A: Journal of Power and Energy*, *224*(7), 969–983. https://doi.org/10.1243/09576509JPE938

Xing, F., Wang, Y. P., & Wang, H. V. (2012). Tidal hydrodynamics and fine-grained sediment transport on the radial sand ridge system in the southern Yellow Sea. *Marine Geology*, *291-294*, 192–210. https://doi.org/10.1016/j.margeo.2011.06.006

Xu, K., Mickey, R. C., Chen, Q., Harris, C. K., Hetland, R. D., Hu, K., & Wang, J. (2016). Shelf sediment transport during hurricanes Katrina and Rita. *Computers and Geosciences*, *90*(B), 24–39. https://doi.org/10.1016/j.cageo.2015.10.009

Young, I. R., Zieger, S., & Babanin, A. V. (2011). Global trends in wind speed and wave height. *Science*, *332*(6028), 451–455. https://doi.org/10.1126/science.1197219

Zhang, W., Cui, Y., Santos, A. I., & Hanebuth, T. J. J. (2016). Storm-driven bottom sediment transport on a high-energy narrow shelf (NW Iberia) and development of mud depocenters. *Journal of Geophysical Research: Oceans*, *121*, 5751–5772. https://doi.org/10.1002/2015JC011526

Zimmerman, J. T. F. (1978). Topographic generation of residual circulation by oscillatory (tidal) currents. *Geophysical and Astrophysical Fluid Dynamics*, *11*(1), 35–47. https://doi.org/10.1080/03091927808242650